

Article

The Age of Hubi Copper (Cobalt) Ore Mineralization in the Zhongtiao Mountain Area, Southern Margin of the Trans-North China Orogen: New Constraints from U-Pb Dating of Rutile and Monazite

Mengqi Wang *, Jingwen Mao *, Huishou Ye and Hongying Li

Key Laboratory of Metallogeny and Mineral Assessment, Institute of Mineral and Resources, Chinese Academy of Geological Sciences, Beijing 100037, China; yehuishou@163.com (H.Y.); lihongying@163.com (H.L.)

* Correspondence: wangmengqi5766@163.com (M.W.); jingwenmao@263.net (J.M.)

Abstract: The Hubi copper (cobalt) ore district, one of the largest typical examples of the sediment-hosted stratiform type in the Zhongtiao Mountain area, is located on the southern margin of the Trans-North China Orogen within the North China Craton (NCC) and has a copper reserve of 0.79 Mt. Mineralization is mainly hosted by the Zhongtiao Group, a sequence of metasedimentary rocks deposited from ~2168 Ma to ~2059 Ma. Subsequently, a collisional orogeny (Trans-North China Orogen) occurred at ~1.85 Ga. The absolute age of mineralization has not been well constrained due to the lack of suitable minerals for dating. Rutile and monazite are common accessory minerals and are intergrown with Cu mineralization in Cu-bearing veins in the Hubi-type copper (cobalt) deposits. This study presents the first new LA-ICP-MS U-Pb ages of hydrothermal rutile and monazite for the Tongmugou and Laobaotan copper (cobalt) deposits in the ore district, which yield lower intercept rutile U-Pb ages of 1815 ± 30 Ma (Mean Squared Weighted Deviation, MSWD = 5.0) and 1858 ± 27 Ma (MSWD = 5.2) for Tongmugou and 1876 ± 30 Ma (MSWD = 5.9) for Laobaotan. Monazite crystals separated from Cu-bearing carbonate veins within the orebody of Tongmugou yield a weighted mean $^{207}\text{Pb}/^{206}\text{Pb}$ age of 1856 ± 14 Ma (MSWD = 1.9), which is close to that of rutile within error. Mineralogical observations and geochemical characteristics suggest that both monazite and rutile crystallized in the hydrothermal fluid system and are closely related to Cu sulfide mineralization. Therefore, their nearly identical U-Pb isotope age of ca. 1850 Ma directly reflects the timing of metamorphic hydrothermal Cu mineralization. This age is indistinguishable from that of metamorphism during the collisional orogeny (Trans-North China Orogen) that led to the final amalgamation of the Eastern and Western Blocks. According to previous studies, the primary sedimentary mineralization of the Hubi-type copper (cobalt) deposits was synchronous with the deposition of the Zhongtiao Group. From the perspective of mineralization age, both the Congolese–Zambian Copperbelt and the Hubi copper (cobalt) ore district experienced early preorogenic sedimentary diagenetic mineralization and late metamorphic hydrothermal mineralization related to orogenesis, and the Hubi-type copper (cobalt) deposits may also be some of the oldest sediment-hosted stratiform-type deposits in the world. Moreover, this metamorphic hydrothermal Cu mineralization spread throughout the Zhongtiao Mountain area.

Keywords: sediment-hosted stratiform copper (cobalt) deposit; age of mineralization; rutile U-Pb dating; monazite U-Pb dating; Trans-North China Orogen



Citation: Wang, M.; Mao, J.; Ye, H.; Li, H. The Age of Hubi Copper (Cobalt) Ore Mineralization in the Zhongtiao Mountain Area, Southern Margin of the Trans-North China Orogen: New Constraints from U-Pb Dating of Rutile and Monazite. *Minerals* **2022**, *12*, 288. <https://doi.org/10.3390/min12030288>

Academic Editor: Georgia Pe-Piper

Received: 20 January 2022

Accepted: 23 February 2022

Published: 25 February 2022

Publisher's Note: MDPI stays neutral with regard to jurisdictional claims in published maps and institutional affiliations.



Copyright: © 2022 by the authors. Licensee MDPI, Basel, Switzerland. This article is an open access article distributed under the terms and conditions of the Creative Commons Attribution (CC BY) license (<https://creativecommons.org/licenses/by/4.0/>).

1. Introduction

The Zhongtiao Mountain area is located in the southern part of the North China Craton (NCC) and has undergone a long period of geological evolution (Figure 1b). In this process, different types of deposits have developed, with proven copper reserves of more than 3.9 million tons, accompanied by ore-forming elements such as cobalt, gold,

molybdenum and silver [1,2]. Therefore, the Zhongtiao Mountain area is also one of the most important copper concentration areas in China.

Within this area, the largest and most attractive deposits are the Tongkuangyu porphyry copper deposit and the Hubi copper (cobalt) ore district, which contains several medium- to large-sized copper (cobalt) deposits in metasedimentary rocks, such as the Tongmugou, Laobaotan, Bizigou and Nanhegou copper (cobalt) deposits (Figure 1a) usually defined as Hubi-type copper (cobalt) deposits in China. According to previous studies and compared with typical strata-controlled deposits that have Cu-Co as the main ore type, the Hubi-type copper (cobalt) deposits reflect a mineralization process that is similar to that of the sediment-hosted stratiform copper-cobalt deposits (SSCs) in the Central African Copperbelt [2].

Sediment-hosted stratiform copper or sedimentary copper deposits are important sources of copper, cobalt and silver [3,4], contributing ~15% of the world's copper resources [5]. Representative superlarge SSC deposits include the Siberian Paleoproterozoic Udokan copper deposit [6,7], the Central African Neoproterozoic Copperbelt [4] and the European Permian Kupferschiefer copper deposit [8]. The low–medium-temperature, oxidizing Cu-rich brine in the basin migrates to the redox interface in the sedimentary layer to cause metal sulfide precipitation, which is a widely accepted genetic model of sediment-hosted stratiform Cu deposits [9–11]. Reliable ages of mineralization for sediment-hosted stratiform Cu deposits are essential for a better understanding of copper deposition and their relationship with regional geological processes such as metamorphism and deformation. However, the age of mineralization is also the most controversial issue and has directly generated academic debates about syndiagenetic [4,10,12,13] or synorogenic timing [14–18], as well as evolution into multistage mineralization [10,11,19–25].

The age of the Hubi copper (cobalt) district in the Zhongtiao Mountain mining district has not been well constrained. On the one hand, some of the research results are from the older literature, when the test methods were not accurate enough; on the other hand, the age is debatable partly because of the lack of suitable dating minerals. It was suggested that the Hubi-type copper (cobalt) deposits formed at 1830 ± 34 Ma based on U-Pb dating of uraninite and brannerite in disseminated and vein ores of the Hubi-type copper (cobalt) deposits [26]. Moreover, uranium mineralization and copper mineralization have an obvious spatial relationship [26]. The authors of [27] reported the Re-Os age of molybdenite associated with a small amount of Cu-bearing sulfide within molybdenite veins along the fault from the Hubi-type copper (cobalt) deposits and obtained the model age of 1901 ± 24 Ma, which was close to the timing of copper mineralization. Recently, chalcopyrite in Cu-bearing quartz veins of the Hubi-type copper (cobalt) deposits yielded a mean model Re-Os age of 1952 ± 39 Ma [28].

Rutile and monazite are common accessory minerals in a wide range of sedimentary, magmatic and metamorphic rocks, and they are considered reliable dating minerals in some hydrothermal ore deposits due to the trace amounts of U in their structure and have a high closure temperature (usually >500 °C) for U-Pb diffusion [29–33]. As a result, these minerals have great potential as U-Pb geochronometers to solve geological issues; U-Pb analysis has been successfully applied in the dating of mineral deposits where rutile and monazite are associated with ore minerals [34–39].

In this study, we carried out laser ablation inductively coupled plasma mass spectrometry (LA-ICP-MS) U-Pb analysis for dating rutile and monazite to determine the mineralization age of the Hubi-type copper (cobalt) deposits. This is the first time that the method has been employed for dating the Hubi-type copper (cobalt) deposits. These new age data also provide constraints on the regional metallogeny and tectonic background.

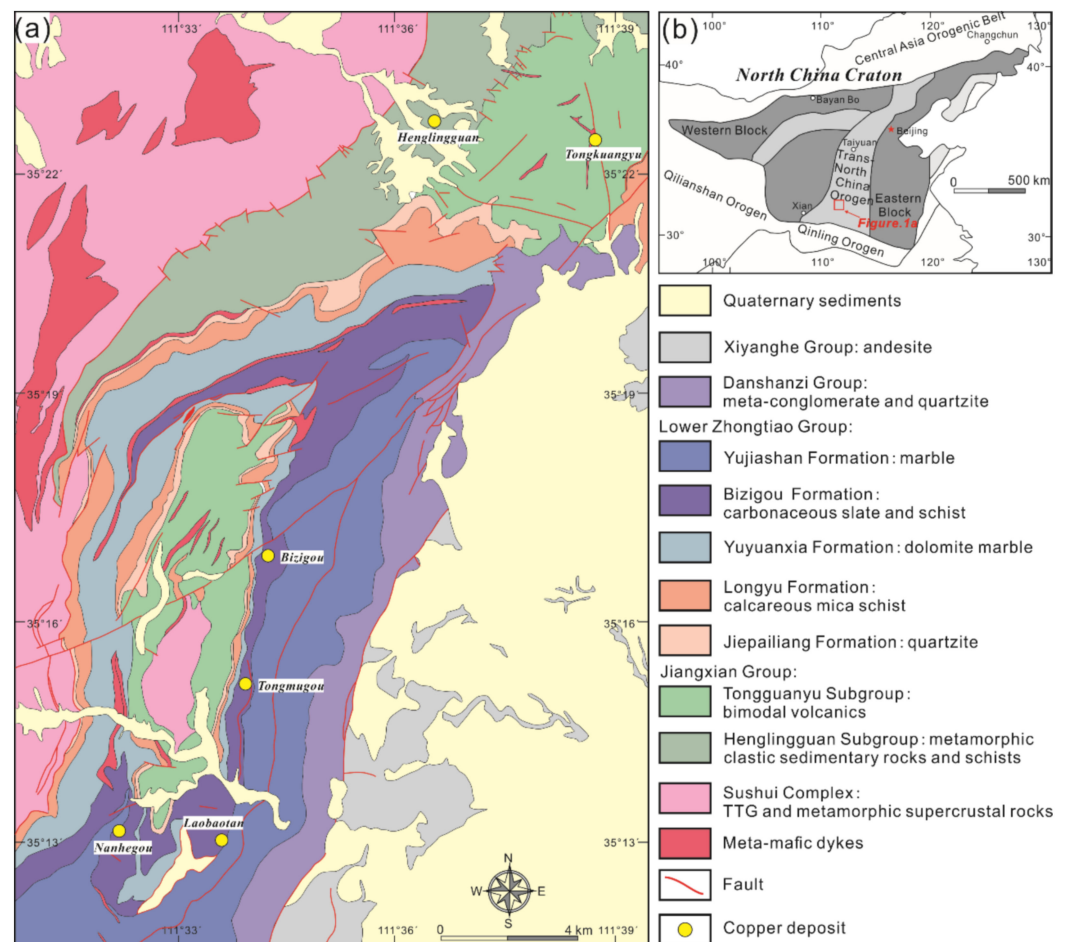


Figure 1. Geological map (a) of the Zhongtiao Mountain area (modified from internal material of the project “Investigation of Key Issues and Mineral Geology Mapping in Zhongtiao Mountain, Shanxi Province”, and [38]), and [38]), with a simplified map (b) of the North China Craton showing the tectonic location of the study area (modified from [40]).

2. Geological Background

2.1. Regional Geology

The North China Craton is composed of several microcontinents, but its tectonic evolution is controversial [40–45]. In recent years, an increasing number of scholars believe that the North China Craton was formed by the collision of the Eastern and Western Blocks along the Trans-North China Orogen [40,41,46–61]. The Zhongtiao Mountain region is located on the southern margin of the Trans-North China Orogen [40,41], and it is one of the hot areas in research on the Precambrian geology of the North China Craton. According to much research on metamorphic petrology, geochronology, geochemistry and tectonic geology in the Trans-North China Orogen, more geological evidence indicates that the collisional orogeny occurred at approximately 1.85 Ga [40,46,53,57–59,62–65].

The relatively complete Precambrian rock tectonic units exposed in the Zhongtiao Mountain region, from bottom to top, can be divided into the Neoproterozoic Sushui Complex, Palaeoproterozoic Jiangxian Group, Zhongtiao Group, Danshanzi Group and Mesoproterozoic Xiyanghe Group (Figure 1a) [66–69]. These rock units generally experienced various degrees of metamorphism except for the Xiyanghe Group.

The Sushui Complex is the oldest rock unit and mainly consists of a series of tonalite-trondhjemite-granodiorite (TTG) gneisses (2.70–2.55 Ga) and metamorphic supercrustal rocks [70,71]. It shows unconformity contacts between the Jiangxian Group and Zhongtiao Group.

The Jiangxian Group contains important ore-bearing strata of the Tongkuangyu porphyry deposit, mainly distributed north of Zhongtiao Mountain. This group can be divided into the Henglingguan Subgroup and Tongkuangyu Subgroup. The Henglingguan Subgroup is a set of metamorphic clastic sedimentary rocks and schists (killas) formed by metamorphism from carbonaceous argillaceous to semi-argillaceous rocks. The Tongkuangyu Subgroup is composed of a set of shallow marine facies clastic rocks and mudstone sedimentary formations in the lower part and a set of marine facies volcanic sedimentary rocks in the upper part. According to previous studies, the formation age of the Jiangxian Group is ca. 2.2 to ~2.1 Ga [2,66,67,72–76].

The Zhongtiao Group crops out widely on the eastern flank of the Shangyupo anticline, which also contains significant ore-bearing strata of the Hubi-type copper (cobalt) deposits. The Zhongtiao Group unconformably covers the Sushui Complex and the Jiangxian Group and comprises a sequence of low-grade metamorphic rock series of sandy-argillaceous and carbonate rocks affected by regional metamorphism, such as quartzite, schist, slate and marble. The total thickness is approximately 6000 m. There have been several studies on the deposition time of the Zhongtiao Group. The result of single-grain zircon U-Pb dating of the metatuff is 2059 ± 5 Ma [68]. The authors of [77] determined that the three youngest detrital zircons defined a weighted mean age of 2168 ± 5 Ma through LA-ICP-MS dating from the quartz schist of the Zhongtiao Group, limiting the maximum sedimentary age. The authors of [76] reported a secondary ionization mass spectrometry (SIMS) zircon U-Pb age of ca. 2168 Ma for the plagioclase amphibolite interlayer of the Zhongtiao Group. In summary, the Zhongtiao Group was deposited from ca. 2168 Ma to 2059 Ma.

The Danshanshi Group is unconformably in contact with the Lower Zhongtiao Group and consists of metaconglomerate and quartzite, which are considered to be molasse formations. The maximum depositional age is ca. 1848 Ma based on detrital zircon U-Pb dating [75].

The Xiyanghe Group, also named the Xiong'er Group in western Henan Province south of the study region, is mainly distributed in the north and south of Zhongtiao Mountain and comprises thick unmetamorphosed andesites that unconformably cover Paleoproterozoic strata. The authors of [78] considered that the formation age of the Xiyanghe Group was approximately 1800–1750 Ma through sensitive high-resolution ion microprobe (SHRIMP) zircon U-Pb dating of volcanic rocks.

The Zhongtiao Mountain region can be divided into three important tectonic movements which affect the deformation and metamorphism: Jiangxian movement (D1), Zhongtiao movement I (D2), Zhongtiao movement II (D3) [67]. D1 led to the unconformity contact between the Jiangxian Group and Zhongtiao Group, mainly in the form of tensile structures. The unconformity contact between the Zhongtiao Group and Danshanshi Group was caused by D2. It is characterized by isoclinal fold and stretching lineation, and the deformation of the Bizigou Formation in the Zhongtiao Group is characterized by strong foliation. D3 resulted in the formation of a broad fold in this region, such as the Shangyupo-Hujiayu anticline [67]. The metamorphism age of D1 is considered to be ca. 2100 Ma, while D2 occurred at ca. 1900 Ma and D3 occurred at ca. 1850 Ma, representing the peak metamorphism age [52,67]. The Zhongtiao Mountain area was generally affected by regional metamorphism of the greenschist facies to amphibolite facies, and the metamorphic temperature spans approximately 350–600 °C [67–69].

2.2. Deposit Geology

The Hubi copper (cobalt) ore district is located on the southeast wing of the Shangyupo-Hujiayu anticline and consists of a series of adjacent copper deposits with similar geological characteristics, including the Tongmugou, Laobaotan, Bizigou and Nanhegou copper deposits (Figure 1a). The copper reserve of the Hubi copper (cobalt) ore district is 0.79 Mt, with an average grade of 1.21%. The Tongmugou and Laobaotan copper deposits are controlled by the Shangyupo anticline structure, so they are distributed in the southeastern part of the anticline in the NNE direction (Figure 1a) and are representative of the Hubi-

type copper (cobalt) deposits. The main economic metal in the two deposits is copper (average grade of 1.08% in Tongmugou and 1.13% in Laobaotan), with by-products of cobalt, molybdenum, gold and silver. The main orebodies are all hosted in the Bizigou Formation but have been affected by post-multiple periods and various structural overprints, and the combinations of surrounding rocks are slightly different.

Regionally, the exposed stratigraphic sequence includes the Jiepailiang, Longyu, Yuyuanxia, Bizigou and Yujiashan Formations (Figure 1a). The Jiepailiang Formation is a set of quartzites, while the lithology of the Longyu Formation is mainly calcareous mica schist. The Bizigou Formation hosts the main ore-bearing strata, which are carbonaceous slate and schist. The upper and lower parts of the strata conformably contact with the marble of the Yujiashan and Yuyuanxia Formations, respectively.

2.3. Tongmugou Copper Deposit

In the Tongmugou copper deposit, the quartzite of the Jiepailiang Formation is regarded as the core of the Tongmugou anticline. In the east limb, the Longyu, Yuyuanxia, Bizigou and Yujiashan Formations appear successively, among which the Longyu and Yuyuanxia Formations are very thin and even partially unexposed (Figure 2a). The lithological composition of the Bizigou Formation in the mining area can be divided into three types: silicic albitite, carbonaceous schist and dolomitic marble (Figure 2a). The orebodies are hosted in the Bizigou Formation on the west limb (Figure 2a). The Tongmugou deposit is composed of many lenticular orebodies of different sizes arranged in parallel, among which the No. 3 orebody is the main one. The reserves of the No. 3 orebody account for more than 70% of the total reserve of the ore district. The No. 3 orebody is approximately 1000 m long, and its thickness varies to a certain extent. It gradually thickens from south to north approximately tens of meters, and the local orebody is lenticular and stratiform with a maximum grade of 13.6% and an average grade of 1.17% and partly controlled by three NNE-trending reverse faults (Figure 2b). Its dip is NW–SE with a dip angle of approximately 40°.

The orebodies are mainly hosted in silicic albitite and dolomitic marble (Figure 2b), and carbonaceous schist is often mineralized by sulfide parallel to foliation, but this mineralization is obviously weaker than the other two. Two different mineralization stages have been recognized: (1) The early mineralization stage (stage I) is characterized by veinlet and disseminated sulfides. The main host rocks of stage I are carbonaceous schist and silicic albitite, and mineralized veins (usually <0.5 cm) are parallel to the foliation (Figure 3a,b,e). The ore minerals are mainly pyrite and pyrrhotite with small amounts of chalcopyrite and cobaltite. Gangue minerals are mostly quartz, dolomite, biotite, graphite and sericite (Figure 4). These minerals can be seen in hand specimens with certain deformation and stretching and exhibit quartz nodules associated with sulfides (Figure 3a). In addition, disseminated sulfides intergrown with quartz grains are observed under the microscope to be directional, elongated and deformed, suggesting that they were probably emplaced during diagenesis. This stage does not constitute the main mineralization stage but may be a source bed that provided a material basis for later mineralization [79]. (2) The late mineralization stage (stage II) is dominated by thick (usually several centimeters to tens of centimeters) sulfide-bearing veins. The ore veins hosted in silicic albitite and dolomitic marble often cross-cut the stratigraphy of the host rock, and the early-stage sulfide-bearing disseminated and ore veins are controlled by extensional tectonic fractures (Figure 3c,d). In this stage, the sulfide content and grade increased, and the grain size of ore and gangue minerals became coarser than that in stage I. The boundaries between the veins and host rock in this stage are continuous and straight, and stage II can be divided into two substages according to the mineral assemblage (Figure 3d,f). Stage II-a is marked by sulfide-quartz (dolomite) veins, and the vein minerals consist of chalcopyrite, pyrite, pyrrhotite and quartz with minor sphalerite, clausthalite, cubanite, siegenite, dolomite and rutile (Figures 3c and 4). The coarser sulfides are disseminated and veined along the fissures of quartz (dolomite) veins, which cut through veins from stage I and foliation of the host rock (Figure 3c,d). Stage II-b

features sulfide-carbonate veins (usually the thickest veins), and its main mineral assemblage is calcite, ferrodolomite, chalcopyrite, pyrite, pyrrhotite and bornite with minor rutile, apatite and monazite (Figure 3d,h,i and Figure 4). In this substage, vein-like mineralization is significant, in which subhedral to anhedral sulfides are massive and disseminated, filling the carbonate veins (Figure 3i).

Previous study shows that the ore-forming fluids of stage I are characterized by high salinity (22–40 wt.% NaCl equiv.) and a moderate temperature (120–280 °C). Meanwhile, stage II is characterized by CO₂ enrichment, high salinity and a high temperature and underwent significant unmixing at a temperature interval of 240–480 °C, and compositions of the ore-forming fluids in stage II are interpreted to be metamorphic hydrothermal solutions [80].

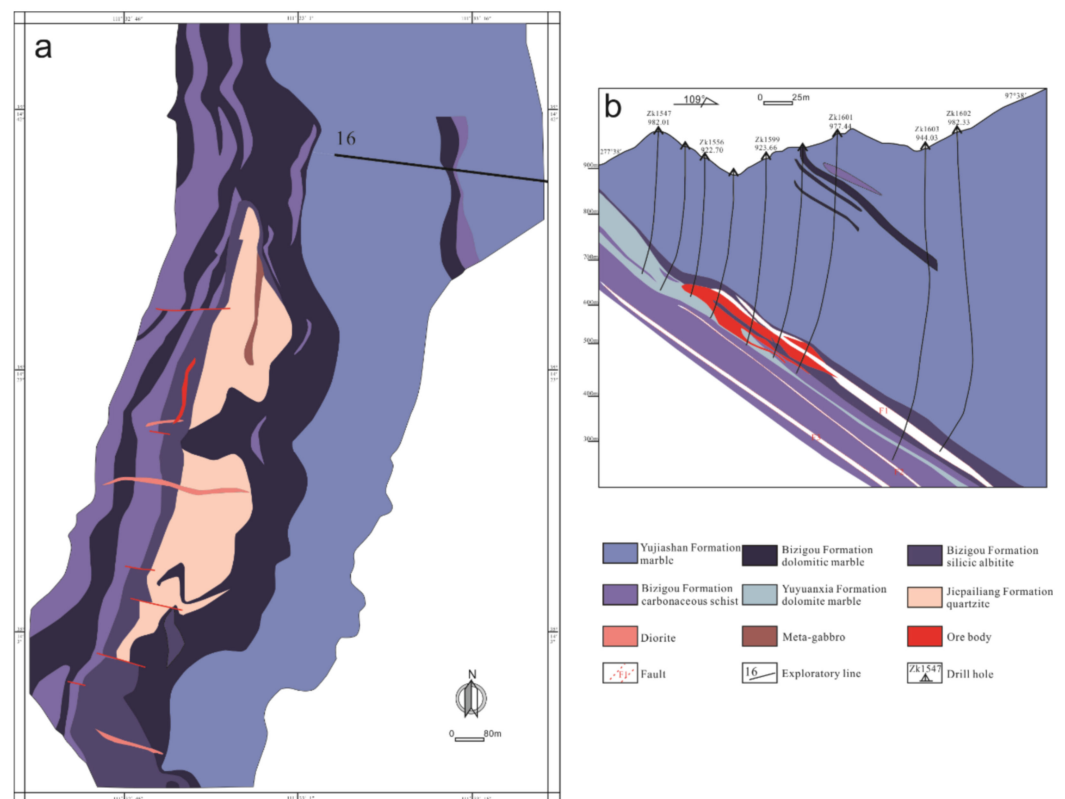


Figure 2. Geological map (a) of the Tongmugou copper deposit, with a geological profile (b) of the No.16 exploration line (modified from internal material of the deposit).

2.4. Laobaotan Copper Deposit

In the Laobaotan copper deposit, the outcropping strata are mainly the Zhongtiao Group, which can be divided into quartzite of the Jiepaijiang Formation, calcareous mica schist of the Longyu Formation, dolomite marble of the Yuyuanxia Formation, carbonaceous schist and silicic marble of the Bizigou Formation and gray marble of the Yujiashan Formation from bottom to top. The structure of the mining area is the Laobaotan anticline, which is a secondary structure in the southeastern Shangyupo-Hujiayu anticline. The core of the Laobaotan anticline is the Jiepaijiang and Longyu Formations, but some areas are barely exposed and even disappear. The flanks of the anticline are mainly composed of different lithologic sections of the Bizigou Formation. The bedded orebodies mainly occur in the Bizigou Formation, and the local mineralization is at the contact between the Bizigou Formation and the lower part of the Yujiashan Formation (Figure 5a). The No. 7 orebody is the main industrial mining orebody. It is approximately 400 m long and can extend to 500 m. The thickness varies greatly (0.7–18.6 m) with an average value of 1.9 m. The orebody formed in layers, lenses and “crescent shapes” on the plane (Figure 5b). Due

to the influence of tectonic activity, the occurrence of the orebody is unstable; it trends SE–NW, and the dip angle is approximately 30°. The copper grade changes obviously, with the highest grade of 21.4% and an average grade of 0.9%, and gradually becomes poor along the trend from NE to SW. Carbonaceous schist and silicic marble are considered the host rocks of the copper ore. According to the field work and previous study, the mineralization type is similar to that of Tongmugou, which can be divided into an early mineralization stage (stage I, diagenetic mineralization) and a late mineralization stage (stage II, metamorphic hydrothermal mineralization). The early diagenetic mineralization is characterized by disseminated veins on a small scale, and the main mineral assemblage is quartz + calcite + dolomite + chalcopyrite + pyrite ± pyrrhotite ± albite ± biotite ± sericite. The fine sulfide-bearing quartz veins are intermittent and nodular along the rock foliation, which may be caused by differential compaction in the diagenetic stage (Figure 6a,d). In the late metamorphic hydrothermal stage mineralization, ore-bearing veins are thick and usually 2–20 cm wide with mineral paragenesis, including quartz + calcite + dolomite ± ankerite + chalcopyrite + pyrite ± biotite (Figure 7). Quartz and calcite often occur as coarse euhedral–subhedral crystals, and chalcopyrite and pyrite are distributed in the cleavage of calcite and quartz intersections as blocky masses (Figure 6e,f). The veins of this stage are obviously controlled by tectonic fractures, cutting through early stage I veins and carbonaceous schist foliation (Figure 6b,c). In general, stage II hydrothermal vein mineralization is also evidently stratabound and limited to the whole stratified orebody, reflecting the affinity and inheritance relationship between the late mineralization and early mineralization and indicating that the migration distance for reactivation of ore-forming elements is not long.

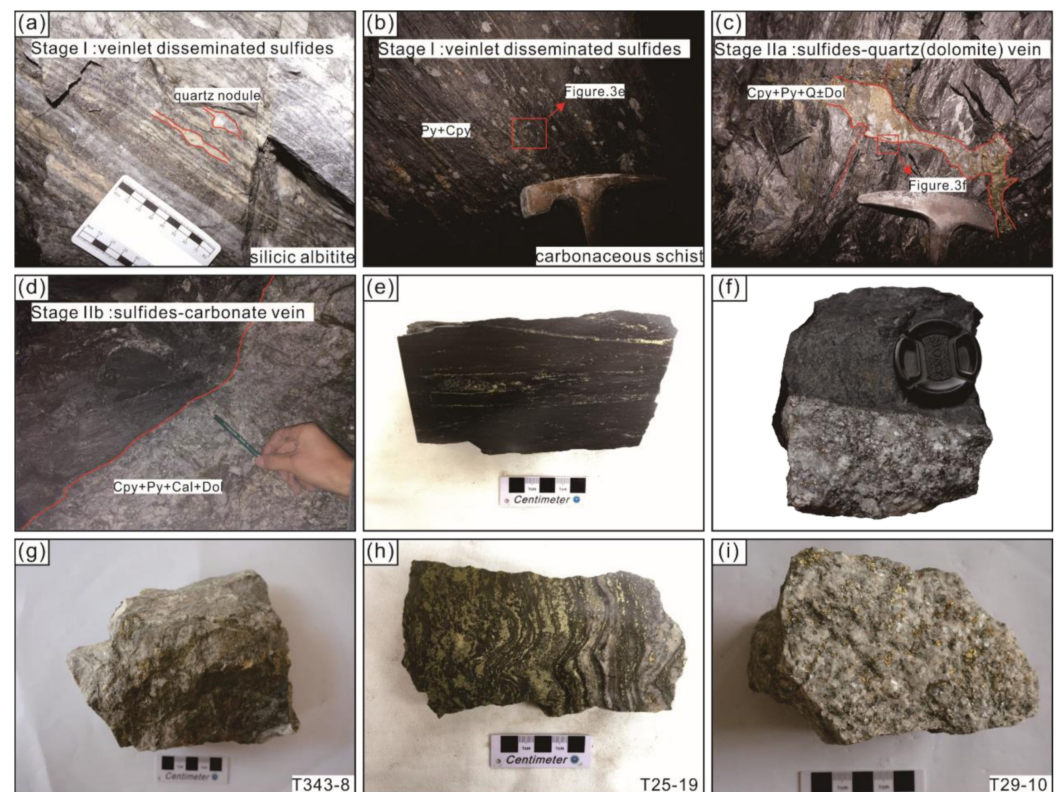


Figure 3. Occurrence of the different stages of mineralization and host rock samples in the Tongmugou deposit. (a,b) Early mineralization stage characterized by veinlet and disseminated sulfides in silicic albite and carbonaceous schist. (c,d) Late mineralization stage metal sulfide veins cross-cut the stratigraphy of the host rock and early mineralization stage veins. (e,f) Ore samples of stages I and II. (g–i) Selected experimental samples of rutile and monazite. Abbreviations: Py = pyrite; Cpy = chalcopyrite; Q = quartz; Dol = dolomite; Cal = calcite.

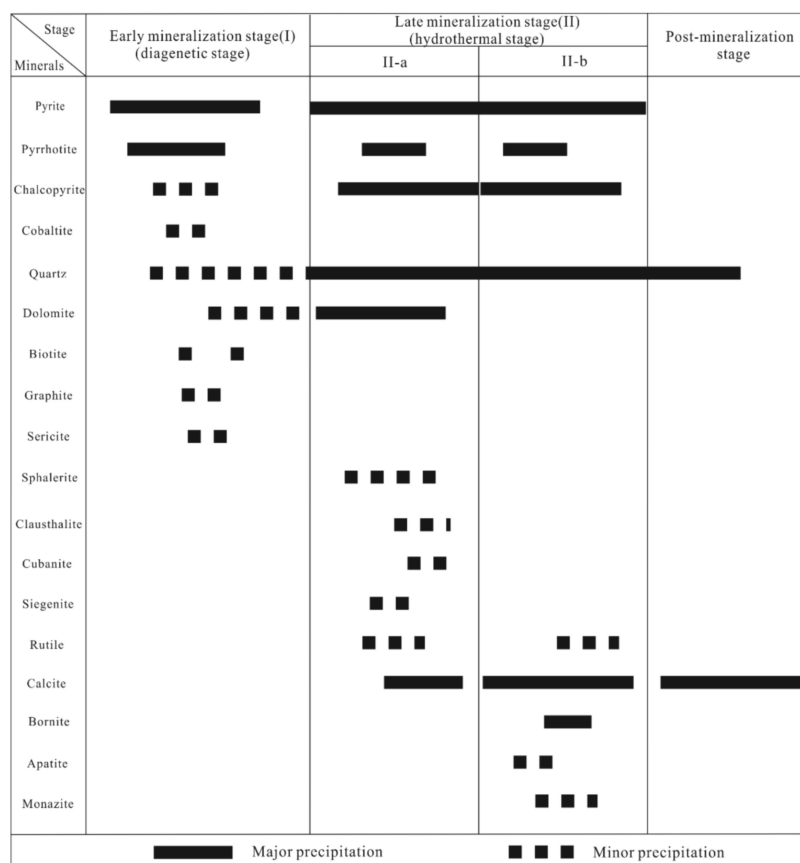


Figure 4. Paragenetic sequence of the Tongmugou deposit.

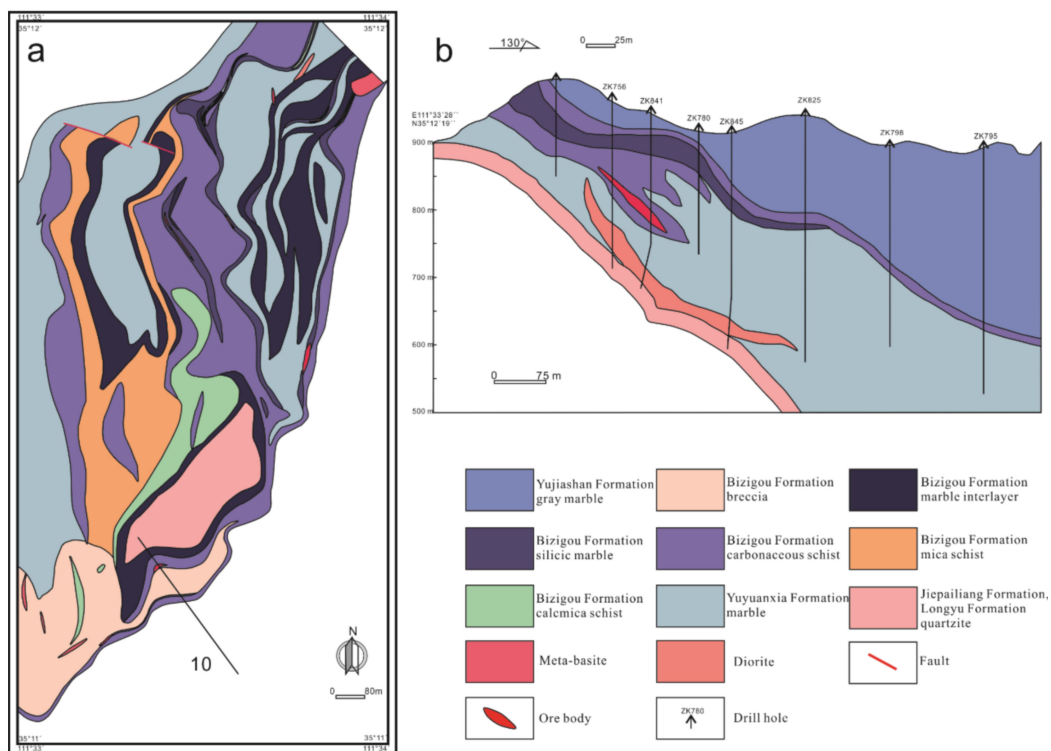


Figure 5. Geological map (a) of the Laobaotan copper deposit, with a geological profile (b) of the No. 10 exploration line (modified from internal material of the deposit).

located by optical microscopy and scanning electron microscopy equipped with energy-dispersive spectrometry (SEM-EDS) to obtain back-scattered electron (BSE) images. The polymorphs of target minerals were analyzed through laser micro-Raman spectroscopy using a Renishaw System-2000 equipped with a 514.50 nm Ar⁺ laser (20 mW incident power) and a full-area charge-coupled device detector. The chemical compositions of the selected minerals were determined by electron microprobe analysis (EPMA) using a JXA-8230. All of the above experiments were conducted at the Institute of Mineral Resources, Chinese Academy of Geological Sciences (CAGS), in Beijing.

The rutile and monazite grains were separated from the veins using heavy liquids and magnetic separation and hand-picked under a microscope. The grains were then prepared as grain mounts (separated grains embedded in epoxy) for isotopic measurements. Photomicrographs and BSE images were used to find crack-free and rutile and monazite grains without inclusions.

The U-Pb geochronology analyses of rutile were conducted by LA-ICP-MS with a Photon Machines Analyte G2 excimer laser ablation system ($\lambda = 193$ nm) and a Thermo Neptune Plus MC-ICP-MS with Jet Interface at the Mineral Exploration Research Centre Isotope Geochemistry Lab, Laurentian University, in Canada. The detailed instrument parameters used for the analyses are summarized in Table 1. Using R10 (1090 Ma) as the primary standard, R19 (489.5 Ma) and Sugluk (1719 ± 14 Ma) were interspersed as unknown samples in order to monitor the external uncertainties. During the dating, the results were 480 ± 45 Ma and 1782 ± 55 Ma for R19 and Sugluk, respectively, which are consistent with the standard reference within error, indicating the results are reliable. Analytical techniques were employed according to [31,81,82]. The U-Pb geochronology analyses of monazite were carried out by LA-ICP-MS with a RESOLUTION LR laser ablation system and Agilent Technologies 7700 \times quadrupole ICP-MS at Nanjing FocuMS Technology Co., Ltd. The 193 nm ArF excimer laser was homogenized by a beam delivery system and focused on the surface of the target minerals with an energy density of 8.0 J/cm². Each acquisition of monazite consisted of a background of 20 s (gas blank) followed by a spot diameter of 33 μ m at a repetition rate of 6 Hz for 40 s. Helium (370 mL/min) was used as a carrier gas to transport the aerosol out of the ablation cell and was mixed with argon (~1.15 L/min) through a T-connector before entering the ICP torch. During the test process, monazite standard 44069 (424.9 Ma) and glass NIST610 were used as external standards for U-Pb dating and trace element calibration, respectively. Raw data reduction was performed offline by ICPMSDataCal software [83,84]. A concordia diagram was created using Isoplot/Exsoftware [85].

Table 1. LA-ICP-MS parameters for rutile U-Pb isotope analyses.

Laser Ablation System	
Make, model and type	Photon Machines, Analyte G2
Ablation cell and volume	Helix II, large format, two volume
Laser wavelength (nm)	193
Pulse width (ns)	<4
Fluence (J.cm-2)	3
Repetition rate (Hz)	7
Ablation duration (secs)	30
Ablation pit depth/ablation rate	~15 μ m/~0.5 μ m/s
Spot size (μ m)	35
Sampling mode/pattern	spot
Carrier gas	He and Ar (after cell) and N ₂ (after cell)
Cell carrier gas flow (L/min)	He1 (cell) = 0.7, He2 (cup) = 0.2, Ar = 0.75, N ₂ = 0.01
ICP-MS Instrument	
Make, model and type	Thermo Neptune Plus with Jet Interface
RF power (W)	1200
Make-up gas flow (L/min)	0.05
Detection system	9 Faraday Cups
Masses measured	²⁰⁴ Pb, ²⁰⁶ Pb, ²⁰⁷ Pb, ²⁰⁸ Pb, ²³² Th, ²³⁸ U
Integration time per peak/dwell times (ms)	NA
Total integration time per output datapoint (secs)	0.25

4. Results

4.1. Rutile Mineralogy and Texture and Composition

Samples T343-8 (sulfide-bearing albite quartz vein, stage II-a), T25-19 (sulfide-bearing carbonate quartz vein, stage II-b) and PD776 (sulfide-bearing quartz vein, stage II) contain a certain amount of rutile intergrown with pyrite and chalcopyrite in the veins from the Tongmugou and Laobaotan deposits. Rutile usually appears as subhedral to anhedral crystals with sizes of 10–200 μm under optical microscopy and scanning electron microscopy, and some rutile crystals show distinct light and dark patchy or oscillatory zoning in BSE images (Figure 8f–h). Partial rutile crystals display relatively homogeneous characteristics; nevertheless, some inclusions are developed on the edges and inside some rutile crystals (Figure 8g).

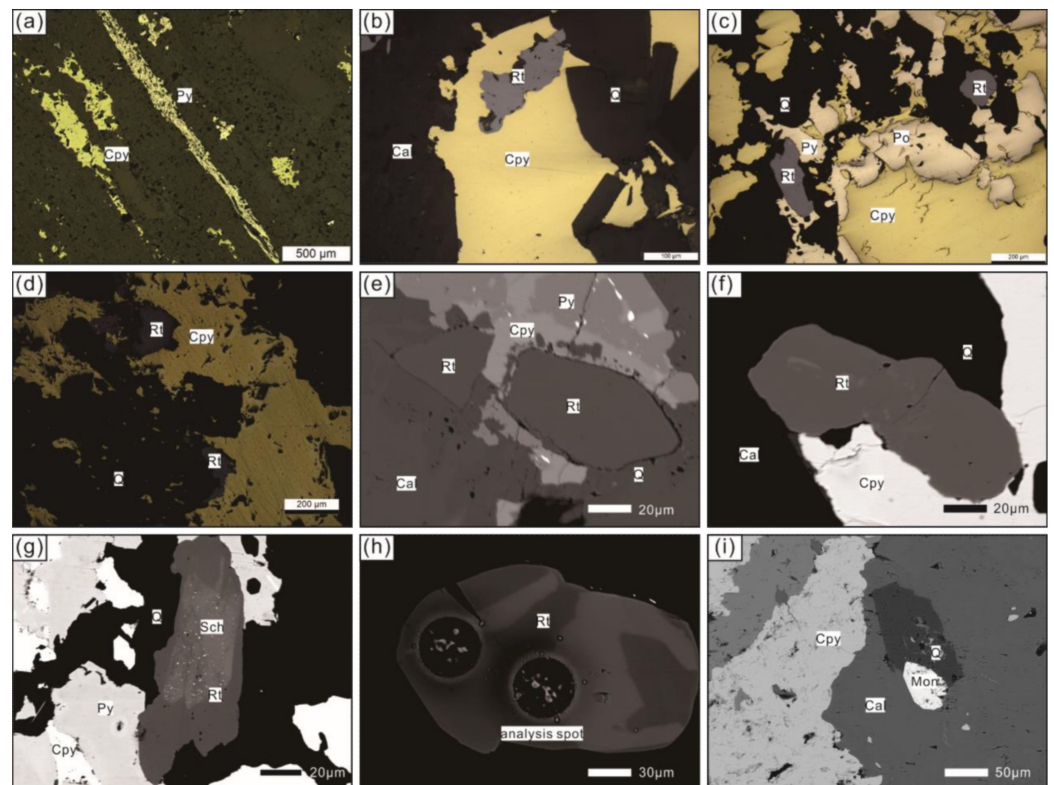


Figure 8. Microphotographs and BSE images of the selected ore samples from the Tongmugou and Laobaotan deposits. (a) Disseminated sulfide veins are directional, elongated and deformed under reflected light. (b–d) Rutile crystals intergrown with sulfides such as chalcopyrite and pyrite in the ore-bearing veins under reflected light. (e) BSE image of the rutile intergrown with sulfides. (f–h) Bright–dark patchy zoning of the rutile crystals and some inclusions are developed inside under BSE. (i) Monazite crystals intergrown with hydrothermal mineral assemblages.

Laser micro-Raman spectroscopy is a technique that can effectively identify mineral polymorphs of TiO_2 minerals such as brookite, anatase and rutile [29]. A compilation of Raman spectra for the three texture TiO_2 polymorphs is shown in Figure 9. Rutile is characterized by four peaks at wavenumbers 143, 247, 447 and 612 cm^{-1} , which can be clearly distinguished from brookite and anatase. The peaks of brookite are mainly 153, 247, 322 and 636 cm^{-1} , while those of anatase are mainly 144, 197, 400, 516 and 640 cm^{-1} [29,86,87]. Laser micro-Raman analysis was performed on the bright and dark zoning of the TiO_2 mineral grains (sample PD776) from sulfide-bearing quartz-carbonate veins (stage II) in this study, and the spectrum shows that the peaks at wavenumbers of 142, 244, 447 and 612 cm^{-1} and 140, 236, 430 and 605 cm^{-1} are most similar to rutile (Figure 9).

Through EPMA, the chemical compositions of the selected rutile crystals from the sulfide-bearing quartz veins are shown in Table 2. Clearly, there are certain differences in the composition of the rutile crystals, which cause the irregular dark and light zoning of the rutile grains. The dark zones of the rutile crystals contain 96.92 to 98.84 wt% TiO_2 , with a mean value of 97.98 wt%, and trace elements including Nb_2O_5 , Cr_2O_3 , FeO , WO_3 and V_2O_3 . The content of Nb_2O_5 is 0.17–0.74 wt%, with a mean value of 0.32 wt%. The abundance of Cr_2O_3 is 0.03–0.36 wt%, with a mean value of 0.19 wt%. The abundance of FeO ranges from 0.07 to 0.52 wt%, with a mean value of 0.33 wt%. The content of WO_3 varies from 0.01 to 0.20 wt%, with a mean value of 0.14 wt%. The content of V_2O_3 ranges from 0.42 to 1.12 wt%, with a mean value of 0.57 wt%. However, the light zoning of the rutile crystals has distinctly lower concentrations of TiO_2 (91.74–96.90 wt%, an average of 93.87 wt%) and evidently higher WO_3 contents (1.24–5.20 wt%, an average of 2.32 wt%). Then, the abundances of FeO (0.63–1.65 wt%, an average of 1.08 wt%) and Nb_2O_5 (0.15–2.66 wt%, an average of 1.25 wt%) are slightly higher than those in the dark zoning. There is little difference in the contents of Cr_2O_3 (0.04–0.65 wt%, an average of 0.33 wt%) and V_2O_3 (0.46–1.21 wt%, an average of 0.74 wt%) between the light and dark zoning of rutile. The concentrations of SiO_2 , Ta_2O_5 and ZrO_2 show no significant differences, and a few of the data are below the detection limit. The authors of [88] compiled electron microprobe (EMP) compositional data of rutile from various Au deposits, and a ternary diagram was developed whereby Ti , $100^* (\text{Fe} + \text{Cr} + \text{V})$ and 1000^*W abundances (Figure 10) were plotted to highlight rutile with anomalous W contents. Above the data plotted on the ternary diagram, it is shown that a majority of the rutile grains plot within ore or sub-ore alteration zones, indicating rutile from ore zones and sub-ore zones had elevated W contents.

4.2. Monazite Mineralogy and Composition

T29-10 is the sample of Cu-bearing carbonate veins (stages II-b), where monazite grains are found within the orebody of the Tongmugou deposit. The mineral assemblage of the mineralization vein is mainly composed of pyrite, chalcopyrite, calcite and quartz (Figure 4). Translucent, colorless monazite crystals are generally associated with stage II-b chalcopyrite in the hydrothermal veins. In the BSE images, monazite crystals are generally homogeneous with sizes of 10–50 μm , and the surfaces are smooth without inclusions, occurring as an accessory mineral associated with chalcopyrite (Figure 8i).

The chemical compositions of the selected monazite grains from the Cu-bearing carbonate veins are shown in Table 3. These partial trace element data were obtained during the LA-ICP-MS U-Pb dating process. Some indicative elements, such as Sc with contents of 0.07–0.30 ppm, Y (3675–11358 ppm), Sm (16563–27464 ppm), Eu (1257–3080 ppm), Gd (8035–13459 ppm), Th (2–378 ppm) and U (209–912 ppm), have Th/U ratios of 0–1.35. Enrichment or depletion of these elements may indicate the origin of monazite.

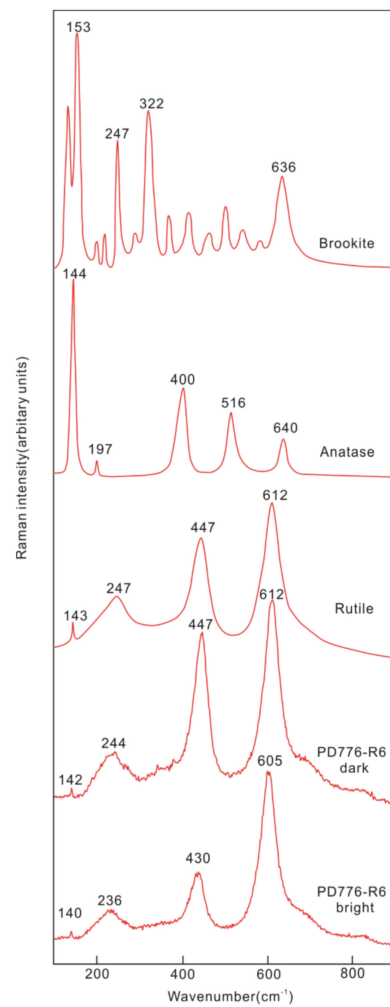


Figure 9. Raman spectra of the TiO₂ polymorphs brookite, anatase, rutile and PD776 from the selected sample.

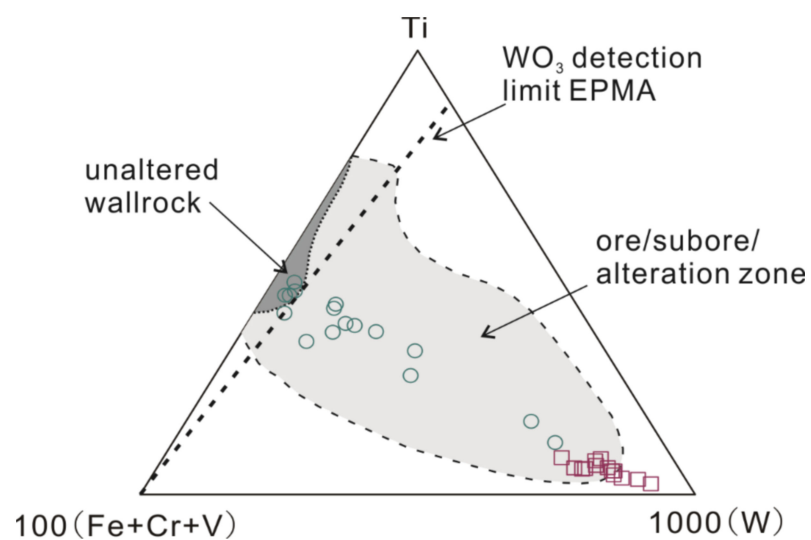


Figure 10. Ternary diagram of W contents in rutile, modified from [88]. The circles and squares are dark zones and bright zones of rutile, respectively.

Table 2. EPMA data of selected rutile crystals from the Tongmugou and Laobaotan copper deposits (wt%).

No.	Comment	SiO ₂	Ta ₂ O ₅	Nb ₂ O ₅	TiO ₂	Cr ₂ O ₃	FeO	ZrO ₂	WO ₃	V ₂ O ₃	Total
1	Dark zoning-1	0.058	0.001	0.19	98.72	0.143	0.343	0.02	0.015	0.547	100.037
2	Dark zoning-2	0.111	0.002	0.284	98.451	0.163	0.318	0.013	0.069	0.556	99.967
3	Dark zoning-3	0.057	0.002	0.367	97.234	0.261	0.452	0.011	0.195	0.558	99.137
4	Dark zoning-4	0.056	0.007	0.296	97.855	0.247	0.318	0.002	0.012	0.477	99.27
5	Dark zoning-5	0.054	0.003	0.737	97.535	0.289	0.37	0.013	0.02	0.527	99.548
6	Dark zoning-6	0.038	0	0.299	98.31	0.116	0.417	0.006	0.077	0.476	99.739
7	Dark zoning-7	0.055	0.003	0.258	97.986	0.145	0.289	0.018	0.048	0.485	99.287
8	Dark zoning-8	0.069	0	0.292	98.059	0.103	0.444	0.002	0.016	0.422	99.407
9	Dark zoning-9	0.021	0	0.175	98.109	0.358	0.311	0.014	0.067	0.507	99.562
10	Dark zoning-10	0.02	0.001	0.202	98.312	0.355	0.489	0.018	0.055	0.553	100.005
11	Dark zoning-11	0.004	0	0.285	98.843	0.285	0.069	0.001	0.05	0.622	100.159
12	Dark zoning-12	0.006	0	0.34	97.382	0.032	0.345	0.006	0.874	1.122	100.107
13	Dark zoning-13	0	0.001	0.223	98.293	0.049	0.235	0.001	0.012	0.638	99.452
14	Dark zoning-14	0.004	0	0.288	97.864	0.057	0.17	0.002	0.098	0.746	99.229
15	Dark zoning-15	0	0	0.508	97.737	0.269	0.268	0.015	0.153	0.426	99.376
16	Dark zoning-16	0.002	0.035	0.398	96.923	0.152	0.521	0.028	0.557	0.482	99.098
17	Light zoning-1	0.062	0	1.267	92.811	0.405	1.132	0.042	3.623	0.601	99.943
18	Light zoning-2	0.056	0	1.373	92.834	0.429	1.317	0.049	2.641	0.65	99.349
19	Light zoning-3	0.049	0	1.319	92.462	0.455	1.472	0.062	3.211	0.666	99.696
20	Light zoning-4	0.071	0	0.92	95.753	0.311	0.741	0.02	1.495	0.598	99.909
21	Light zoning-5	0.05	0.029	2.601	92.497	0.533	1.302	0.03	1.846	0.602	99.49
22	Light zoning-6	0.047	0.027	2.593	92.508	0.587	1.447	0.042	1.761	0.624	99.636
23	Light zoning-7	0.06	0.112	1.806	93.988	0.322	1.169	0.025	1.237	0.576	99.295
24	Light zoning-8	0.068	0	0.145	96.899	0.16	0.776	0.023	1.443	0.494	100.008
25	Light zoning-9	0.013	0	0.649	95.594	0.035	0.817	0.013	1.754	1.113	99.988
26	Light zoning-10	0.003	0	0.395	95.163	0.136	0.786	0.014	2.246	1.034	99.777
27	Light zoning-11	0.001	0	0.387	94.721	0.127	0.691	0.019	2.223	1.208	99.377
28	Light zoning-12	0	0	0.369	95.114	0.111	0.629	0.016	1.937	1.101	99.277

Table 2. Cont.

No.	Comment	SiO ₂	Ta ₂ O ₅	Nb ₂ O ₅	TiO ₂	Cr ₂ O ₃	FeO	ZrO ₂	WO ₃	V ₂ O ₃	Total
29	Light zoing-13	0	0	0.958	91.741	0.645	1.248	0.052	5.202	0.456	100.302
30	Light zoing-14	0.008	0.067	2.659	92.145	0.324	1.653	0.034	1.877	0.593	99.36

Table 3. LA-ICP-MS trace element data of selected monazite crystals from the Tongmugou copper deposit (ppm).

No.	Sc	Y	Zr	Nb	Sm	Eu	Gd	Tb	Dy	Ho	Er	Tm	Yb	Lu	Hf	Ta	Pb	Th	U	Th/U
T29-10-01	0.17	3675	1.21	0.06	20175	1335	8579	556	1762	224	324	20	59	4	0.29	0.04	122	378	280	1.35
T29-10-02	0.12	8050	1.01	0.03	16563	1533	9264	797	3219	473	750	52	168	12	0.48	0.09	188	272	514	0.53
T29-10-03	0.20	11358	0.89	0.04	25106	2042	13459	1131	4393	639	1078	79	263	18	0.69	0.11	139	35	424	0.08
T29-10-04	0.15	9943	1.29	0.05	23915	3052	12502	1100	4242	583	893	57	165	9	0.61	0.10	262	26	815	0.03
T29-10-05	0.30	5300	1.42	0.05	16765	1920	8381	648	2379	325	470	29	81	5	0.38	0.06	83	212	209	1.02
T29-10-06	0.26	10470	1.03	0.05	20350	3080	11267	1039	4255	621	999	68	208	13	0.69	0.12	294	12	912	0.01
T29-10-07	0.18	9717	1.19	0.06	21271	2959	12038	1081	4160	575	907	61	182	10	0.59	0.11	259	2	805	0.00
T29-10-08	0.14	5821	1.17	0.05	27464	1957	13189	907	2819	351	499	30	86	5	0.44	0.06	143	42	430	0.10
T29-10-09	0.14	4906	1.24	0.05	19026	1382	8784	630	2188	295	438	28	84	5	0.28	0.06	163	261	441	0.59
T29-10-10	0.07	4609	1.56	0.09	17922	1257	8035	569	1987	274	419	27	87	6	0.32	0.06	157	354	404	0.88

4.3. Age of Rutile U-Pb Dating

T343-8 and T25-9 represent typical samples of metamorphic hydrothermal mineralization (stage II) in the Tongmugou deposit, while PD776 represents a sample of the Laobaotan deposit in the same mineralization stage. The U-Pb data are listed in Table 4 and presented on Tera–Wasserburg diagrams (Figure 11). Sample T343-8 contains a population of rutile intergrown with chalcopyrite and pyrite in sulfide-bearing albite quartz veins from the Tongmugou deposit, and 36 analyses of 33 rutile grains yielded a lower intercept age of 1815 ± 30 Ma (MSWD = 5.0, N = 36) (Figure 11a). Sample T25-9 includes a number of rutile crystals intergrown with chalcopyrite, while pyrite occurs in sulfide-bearing carbonate quartz veins from the Tongmugou deposit, and 36 analyses of 32 rutile grains yielded a lower intercept age of 1858 ± 27 Ma (MSWD = 5.2, N = 36) (Figure 11b). Forty-one analyses of thirty-seven rutile grains yielded a similar lower intercept age of 1876 ± 30 Ma (MSWD = 5.9, N = 41) (Figure 11c) in sample PD776, which are intergrown with chalcopyrite and pyrite in sulfide-bearing quartz veins from the Laobaotan deposit.

Taken together, all the rutile age data indicate crystallization as a hydrothermal alteration mineral during the metamorphic hydrothermal mineralization event at ca. 1.85 Ga.

Table 4. LA-ICP-MS U-Pb data of rutile from the Tongmugou and Laobaotan copper deposits.

Sample No.	Isotopic Ratios						Apparent Age (Ma)					
	²⁰⁷ Pb/ ²⁰⁶ Pb	2σ	²⁰⁷ Pb/ ²³⁵ U	2σ	²⁰⁶ Pb/ ²³⁸ U	2σ	²⁰⁷ Pb/ ²⁰⁶ Pb	2σ	²⁰⁷ Pb/ ²³⁵ U	2σ	²⁰⁶ Pb/ ²³⁸ U	2σ
Rutile T343-8												
T343-8-1	0.3557	0.0094	31.5	1.7	0.636	0.022	3720	39	3530	53	3164	87
T343-8-2	0.1367	0.0016	6.552	0.21	0.3466	0.0094	2181	18	2050	28	1919	46
T343-8-3	0.1112	0.0036	5.26	0.24	0.348	0.01	1823	40	1859	38	1929	51
T343-8-4	0.113	0.0016	5.076	0.16	0.3251	0.0091	1845	17	1828	27	1813	44
T343-8-5	0.1132	0.0029	5.26	0.21	0.345	0.012	1856	28	1858	36	1909	55
T343-8-6	0.1136	0.0024	4.99	0.18	0.3236	0.0093	1855	22	1812	30	1806	45

Table 4. Cont.

Sample No.	Isotopic Ratios						Apparent Age (Ma)					
	$^{207}\text{Pb}/^{206}\text{Pb}$	2σ	$^{207}\text{Pb}/^{235}\text{U}$	2σ	$^{206}\text{Pb}/^{238}\text{U}$	2σ	$^{207}\text{Pb}/^{206}\text{Pb}$	2σ	$^{207}\text{Pb}/^{235}\text{U}$	2σ	$^{206}\text{Pb}/^{238}\text{U}$	2σ
Rutile T343-8												
T343-8-7	0.119	0.0033	5.21	0.22	0.3179	0.0097	1941	35	1839	36	1777	47
T343-8-8	0.1132	0.0024	5.08	0.18	0.3252	0.0089	1839	25	1827	29	1814	43
T343-8-9	0.2093	0.0071	11.55	0.56	0.3927	0.013	2886	43	2545	45	2131	61
T343-8-10	0.1201	0.0015	5.596	0.17	0.3367	0.0092	1956	16	1912	27	1870	44
T343-8-11	0.1162	0.0052	5.44	0.31	0.3318	0.011	1877	54	1869	43	1845	53
T343-8-12	0.1143	0.0052	4.87	0.25	0.3142	0.01	1811	52	1769	44	1758	50
T343-8-13	0.1482	0.0027	6.85	0.24	0.3327	0.0094	2315	29	2082	31	1850	46
T343-8-14	0.1223	0.0023	5.31	0.2	0.3177	0.01	1977	28	1867	32	1775	49
T343-8-15	0.1467	0.0065	6.69	0.42	0.3327	0.011	2233	63	2036	51	1852	53
T343-8-16	0.1869	0.0088	10.46	0.88	0.384	0.014	2654	66	2386	59	2087	63
T343-8-17	0.268	0.01	19.9	1.4	0.51	0.019	3256	57	3006	65	2650	80
T343-8-18	0.1385	0.0028	6.46	0.25	0.336	0.0096	2198	31	2028	33	1866	46
T343-8-19	0.113	0.0018	5.047	0.17	0.3238	0.0095	1840	18	1823	28	1806	46
T343-8-20	0.12	0.0058	5.52	0.31	0.3356	0.011	1910	61	1878	48	1861	53
T343-8-21	0.1261	0.0061	6.26	0.37	0.3605	0.013	1988	64	1962	54	1981	64
T343-8-22	0.1139	0.0017	5.035	0.16	0.3203	0.0089	1860	17	1821	27	1792	43
T343-8-23	0.1688	0.0027	8.46	0.31	0.3604	0.011	2535	24	2274	33	1982	50
T343-8-24	0.1498	0.0032	7.11	0.27	0.3479	0.0099	2333	31	2115	34	1923	47
T343-8-25	0.1136	0.0023	4.81	0.17	0.3058	0.0089	1860	21	1778	30	1721	43
T343-8-26	0.2972	0.0092	22.9	1.6	0.543	0.023	3429	47	3183	63	2780	91
T343-8-27	0.12084	0.0012	5.601	0.18	0.3328	0.0094	1966	16	1913	27	1851	45
T343-8-28	0.1142	0.0037	5.1	0.22	0.3267	0.0099	1853	39	1824	37	1820	48
T343-8-29	0.2422	0.0095	14.36	0.9	0.4159	0.014	3081	61	2724	57	2241	63
T343-8-30	0.1253	0.0027	5.96	0.23	0.3436	0.0096	2023	30	1959	33	1902	46
T343-8-31	0.1231	0.0032	6.02	0.28	0.3508	0.011	1989	40	1958	38	1936	50
T343-8-32	0.1489	0.0038	7.61	0.4	0.3606	0.012	2319	41	2167	45	1982	56
T343-8-33	0.1218	0.002	6.2	0.21	0.3594	0.01	1985	19	2001	31	1978	49
T343-8-34	0.1157	0.0026	5.18	0.18	0.3264	0.0093	1881	27	1841	31	1820	45
T343-8-35	0.1131	0.0042	5.28	0.25	0.3491	0.012	1839	43	1856	40	1928	56
T343-8-36	0.1417	0.0015	7.12	0.25	0.3626	0.011	2245	15	2119	31	1992	50
Rutile T25-19												
T25-19-1	0.1218	0.0018	5.66	0.19	0.3347	0.0097	1985	19	1921	29	1859	47
T25-19-2	0.2098	0.0098	10.85	0.8	0.3655	0.012	2842	67	2449	60	2002	58
T25-19-3	0.1211	0.0038	5.82	0.24	0.3507	0.011	1968	37	1939	36	1934	52
T25-19-4	0.119	0.0036	5.41	0.23	0.3278	0.01	1935	34	1872	37	1827	51
T25-19-5	0.1261	0.002	5.78	0.19	0.3353	0.0095	2034	24	1938	28	1863	45
T25-19-6	0.112	0.0015	5	0.16	0.3252	0.0091	1828	17	1817	27	1814	44
T25-19-7	0.1282	0.0038	5.88	0.26	0.3289	0.0094	2055	41	1941	35	1832	45
T25-19-8	0.583	0.01	66.3	3.5	0.805	0.035	4455	25	4224	52	3780	120
T25-19-9	0.1524	0.0025	7.33	0.25	0.3469	0.0094	2364	24	2145	30	1919	45
T25-19-10	0.585	0.022	81.9	7.8	0.935	0.066	4382	66	4370	110	4200	220
T25-19-11	0.292	0.012	19.3	1.4	0.457	0.016	3358	63	2975	66	2424	70
T25-19-12	0.1218	0.0018	5.64	0.19	0.3365	0.0098	1984	18	1917	30	1867	47

Table 4. Cont.

Sample No.	Isotopic Ratios						Apparent Age (Ma)					
	$^{207}\text{Pb}/^{206}\text{Pb}$	2σ	$^{207}\text{Pb}/^{235}\text{U}$	2σ	$^{206}\text{Pb}/^{238}\text{U}$	2σ	$^{207}\text{Pb}/^{206}\text{Pb}$	2σ	$^{207}\text{Pb}/^{235}\text{U}$	2σ	$^{206}\text{Pb}/^{238}\text{U}$	2σ
Rutile T25-19												
T25-19-13	0.113	0.0012	4.975	0.16	0.3169	0.0092	1848	14	1814	28	1773	44
T25-19-14	0.1174	0.0025	5.17	0.19	0.3186	0.0095	1907	29	1841	33	1781	46
T25-19-15	0.1254	0.0025	6.27	0.22	0.3707	0.011	2028	24	2011	32	2031	53
T25-19-16	0.1303	0.0043	6.26	0.27	0.356	0.011	2080	43	2007	40	1963	54
T25-19-17	0.1312	0.0031	6.23	0.25	0.3477	0.011	2103	31	1999	36	1919	53
T25-19-18	0.1283	0.0044	6.04	0.34	0.3441	0.011	2088	58	1966	44	1911	50
T25-19-19	0.511	0.012	48	3	0.655	0.03	4261	35	3905	63	3239	120
T25-19-20	0.1188	0.0023	5.27	0.19	0.3213	0.009	1934	26	1858	30	1797	44
T25-19-21	0.1173	0.0026	5.08	0.18	0.3178	0.0094	1910	28	1828	32	1777	46
T25-19-22	0.1161	0.0025	5.56	0.2	0.3504	0.01	1890	28	1902	32	1934	50
T25-19-23	0.259	0.011	15.5	1.1	0.43	0.016	3192	65	2801	63	2297	69
T25-19-24	0.2056	0.0053	10.26	0.43	0.3639	0.011	2861	41	2445	39	2001	55
T25-19-25	0.121	0.0036	5.82	0.25	0.3508	0.011	1956	38	1933	36	1935	53
T25-19-26	0.2509	0.0091	14.34	0.86	0.4079	0.013	3172	55	2750	57	2203	61
T25-19-27	0.1281	0.0037	6.11	0.26	0.358	0.011	2061	39	1988	37	1971	54
T25-19-28	0.1494	0.0041	7.57	0.32	0.3649	0.011	2328	37	2176	38	2003	53
T25-19-29	0.1286	0.0038	5.99	0.25	0.331	0.0096	2072	40	1967	37	1842	46
T25-19-30	0.1629	0.0044	7.93	0.36	0.3517	0.01	2471	39	2209	39	1941	49
T25-19-31	0.45	0.012	35.8	2.1	0.573	0.023	4060	38	3628	57	2904	89
T25-19-32	0.327	0.015	21.9	1.8	0.465	0.022	3525	73	3082	82	2442	91
T25-19-33	0.377	0.017	25.9	2.2	0.484	0.022	3779	66	3305	79	2547	99
T25-19-34	0.1293	0.0024	5.93	0.22	0.3421	0.011	2087	23	1962	32	1895	53
T25-19-35	0.1518	0.0047	7.47	0.34	0.3589	0.011	2347	46	2152	38	1975	49
T25-19-36	0.2308	0.0079	13.09	0.74	0.4106	0.013	3011	50	2656	51	2217	60
Rutile PD776												
PD776-1	0.1109	0.005	4.81	0.25	0.3163	0.01	1783	56	1761	45	1767	51
PD776-2	0.1116	0.0072	4.83	0.33	0.3255	0.011	1781	71	1751	61	1811	55
PD776-3	0.1153	0.0068	5.12	0.32	0.3306	0.012	1840	82	1808	57	1834	59
PD776-4	0.1236	0.0092	5.49	0.45	0.327	0.013	1949	86	1844	67	1816	63
PD776-5	0.1126	0.0072	5.02	0.35	0.3293	0.013	1815	68	1783	60	1826	62
PD776-6	0.1111	0.0038	4.81	0.22	0.319	0.0099	1798	43	1770	39	1782	48
PD776-7	0.1133	0.005	5.11	0.27	0.3335	0.011	1822	50	1805	45	1851	53
PD776-8	0.1143	0.0049	5.05	0.25	0.3246	0.0099	1827	55	1801	44	1812	49
PD776-9	0.1115	0.0048	5.05	0.25	0.3305	0.011	1817	46	1802	43	1840	52
PD776-10	0.1143	0.007	5.07	0.35	0.3304	0.011	1817	81	1810	57	1835	54
PD776-11	0.121	0.0055	5.49	0.3	0.3356	0.011	1923	59	1869	49	1862	51
PD776-12	0.1151	0.006	5.14	0.3	0.3326	0.012	1846	59	1809	51	1844	57
PD776-13	0.129	0.011	5.67	0.55	0.338	0.019	2084	65	1914	80	1877	92
PD776-14	0.1123	0.0078	5.01	0.35	0.3323	0.013	1801	87	1760	69	1843	60
PD776-15	0.1114	0.005	5.22	0.28	0.3448	0.011	1806	58	1841	49	1917	52
PD776-16	0.1148	0.0067	5.37	0.33	0.3505	0.012	1822	67	1845	54	1930	59
PD776-17	0.1133	0.006	5.26	0.31	0.3409	0.012	1843	64	1840	50	1885	56
PD776-18	0.1366	0.0059	6.77	0.35	0.3707	0.013	2141	52	2052	46	2026	60

Table 4. Cont.

Sample No.	Isotopic Ratios						Apparent Age (Ma)					
	$^{207}\text{Pb}/^{206}\text{Pb}$	2σ	$^{207}\text{Pb}/^{235}\text{U}$	2σ	$^{206}\text{Pb}/^{238}\text{U}$	2σ	$^{207}\text{Pb}/^{206}\text{Pb}$	2σ	$^{207}\text{Pb}/^{235}\text{U}$	2σ	$^{206}\text{Pb}/^{238}\text{U}$	2σ
Rutile PD776												
PD776-19	0.1171	0.0065	5.62	0.36	0.3543	0.012	1847	76	1865	55	1949	57
PD776-20	0.113	0.0035	5.45	0.24	0.3528	0.011	1842	38	1881	37	1944	51
PD776-21	0.467	0.037	64	12	0.86	0.1	3630	110	3710	160	3620	290
PD776-22	0.1144	0.0057	5.64	0.31	0.3632	0.013	1833	62	1879	52	1991	60
PD776-23	0.1179	0.007	5.6	0.33	0.3556	0.013	1887	62	1895	51	1958	61
PD776-24	0.1121	0.0059	5.44	0.33	0.3574	0.013	1821	68	1869	54	1968	61
PD776-25	0.219	0.05	10.3	1.5	0.419	0.033	2800	160	2330	140	2180	150
PD776-26	0.1122	0.0058	5.28	0.29	0.3443	0.012	1814	64	1830	53	1901	57
PD776-27	0.114	0.0043	5.64	0.27	0.3651	0.011	1855	43	1912	41	2004	52
PD776-28	0.1131	0.0063	5.53	0.33	0.3601	0.013	1806	69	1860	58	1976	60
PD776-29	0.1246	0.0073	6.32	0.42	0.371	0.012	1980	81	1979	63	2029	57
PD776-30	0.1096	0.0061	4.85	0.3	0.3149	0.012	1773	74	1764	56	1766	61
PD776-31	0.1105	0.0059	4.68	0.26	0.3142	0.011	1781	60	1731	49	1757	52
PD776-32	0.1186	0.0066	5.22	0.35	0.3194	0.01	1871	66	1806	51	1782	51
PD776-33	0.1097	0.0059	5.27	0.31	0.3425	0.012	1784	66	1816	54	1892	58
PD776-34	0.109	0.011	4.87	0.49	0.323	0.015	1830	110	1734	85	1797	76
PD776-35	0.1597	0.0088	7.64	0.53	0.3519	0.013	2344	79	2129	65	1936	60
PD776-36	0.123	0.012	5.45	0.54	0.337	0.017	2060	110	1874	80	1862	81
PD776-37	0.1163	0.006	5.3	0.31	0.3306	0.012	1857	65	1827	54	1835	57
PD776-38	0.169	0.017	7.76	0.66	0.373	0.02	2410	100	2148	83	2027	92
PD776-39	0.116	0.0056	5.22	0.29	0.3288	0.012	1856	50	1829	49	1826	57
PD776-40	0.1259	0.0091	5.3	0.38	0.319	0.013	1965	88	1807	71	1778	67
PD776-41	0.1201	0.0059	5.26	0.28	0.3215	0.01	1921	59	1829	49	1793	51

4.4. Age of Monazite U-Pb Dating

The U-Pb isotope analyses of monazite from sample T29-10 are summarized in Table 5. The monazite grains have a U content of 209–912 ppm and a Th concentration of 2–378 ppm, giving Th/U ratios of 0–1.35. Monazite grains occur as euhedral to subhedral grains, with a size of 40–120 μm . The surface of the grains is smooth and does not show light–dark patchy or oscillatory zoning in the BSE images. Ten analyses of ten monazite grains yielded a concordia age of 1846 ± 3 Ma (MSWD = 5.5, N = 10) (Figure 12a), a lower intercept age of 1841 ± 3 Ma (MSWD = 0.62, N = 10) (Figure 12b) and a weighted mean $^{207}\text{Pb}/^{206}\text{Pb}$ age of 1856 ± 14 Ma (MSWD = 1.9, N = 9) (Figure 12c), which is close to that of rutile mentioned above. The monazite age data suggest that the metamorphic hydrothermal mineralization event probably occurred at approximately 1.85 Ga.

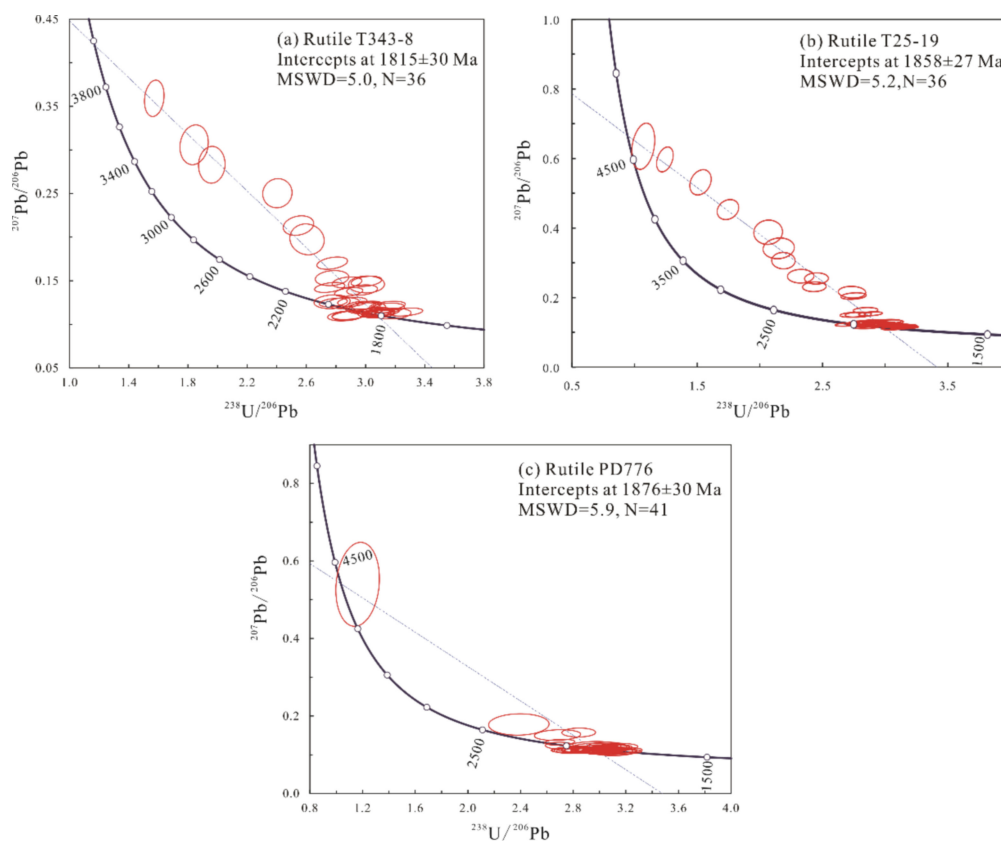


Figure 11. Tera–Wasserburg diagrams of rutile. (a) Sample T343-8 in sulfide-bearing albite quartz veins from the Tongmugou deposit. (b) Sample T25-9 in sulfide-bearing carbonate quartz veins from the Tongmugou deposit. (c) Sample PD776 in sulfide-bearing quartz veins from the Laobaotan deposit.

Table 5. LA-ICP-MS U-Pb data of monazite from the Tongmugou copper deposit.

Sample No.	Isotopic Ratios							Apparent Age (Ma)					
	$^{207}\text{Pb}/^{206}\text{Pb}$	1σ	$^{207}\text{Pb}/^{235}\text{U}$	1σ	$^{206}\text{Pb}/^{238}\text{U}$	1σ	<i>rho</i>	$^{207}\text{Pb}/^{206}\text{Pb}$	1σ	$^{207}\text{Pb}/^{235}\text{U}$	1σ	$^{206}\text{Pb}/^{238}\text{U}$	1σ
T29-10-1	0.1120	0.0010	5.0919	0.0706	0.3352	0.0024	0.5165	1832	18	1835	12	1864	12
T29-10-2	0.1120	0.0007	5.0785	0.0607	0.3341	0.0021	0.5179	1832	12	1833	10	1858	10
T29-10-3	0.1126	0.0008	5.0758	0.0607	0.3323	0.0021	0.5366	1843	12	1832	10	1849	10
T29-10-4	0.1139	0.0008	5.1499	0.0745	0.3325	0.0029	0.5935	1863	13	1844	12	1850	14
T29-10-5	0.1132	0.0013	5.1126	0.0863	0.3325	0.0030	0.5318	1854	21	1838	14	1850	14
T29-10-6	0.1147	0.0008	5.1863	0.0668	0.3326	0.0024	0.5493	1876	11	1850	11	1851	11
T29-10-7	0.1147	0.0008	5.1415	0.0683	0.3300	0.0025	0.5658	1876	13	1843	11	1838	12
T29-10-8	0.1128	0.0009	5.1195	0.0651	0.3345	0.0021	0.4945	1844	13	1839	11	1860	10
T29-10-9	0.1144	0.0009	5.1436	0.0713	0.3310	0.0025	0.5418	1870	13	1843	12	1843	12
T29-10-10	0.1174	0.0010	5.2448	0.0762	0.3293	0.0030	0.6313	1916	15	1860	12	1835	15

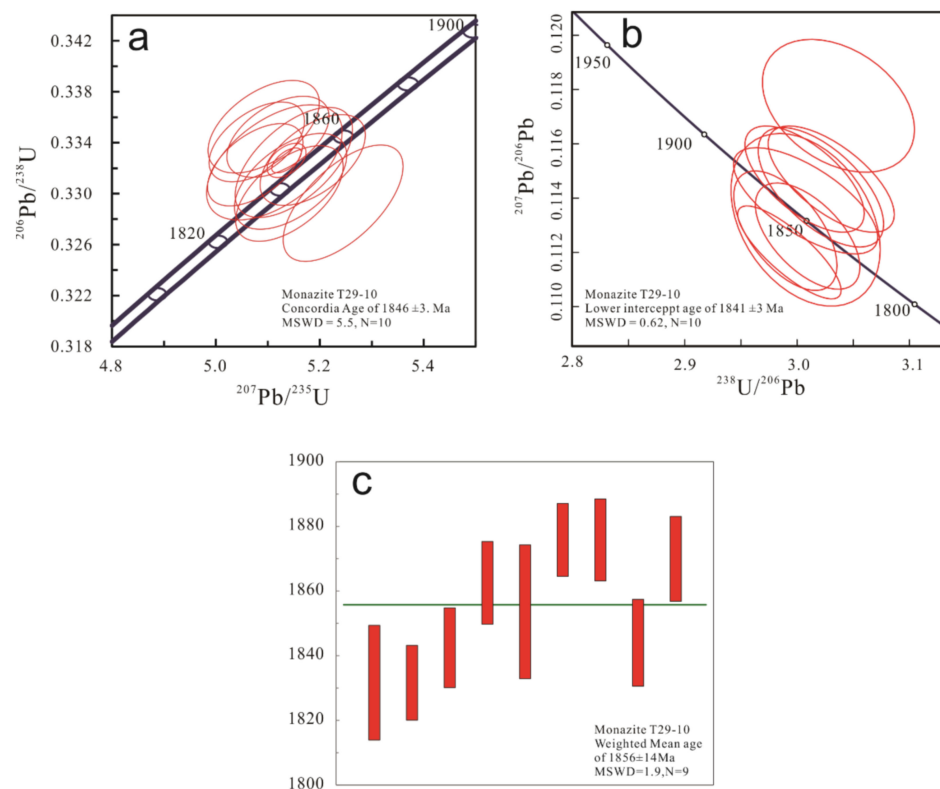


Figure 12. Concordia diagram (a), Tera–Wasserburg plot (b) and weighted mean $^{207}\text{Pb}/^{206}\text{Pb}$ age (c) of monazite from sample T29-10 in Cu-bearing carbonate veins from the Tongmugou deposit.

5. Discussion

5.1. Origin of Monazite and Rutile

U-bearing accessory minerals such as zircon, monazite and rutile are widely distributed in various types of rocks and ore deposits, and their U-Pb ages can be used to constrain the ages of geological events [89]. Regardless of magmatic, hydrothermal or sedimentary origin, the identification of monazite genetic types restricts the reasonable interpretation of geological age [90–92]. Hydrothermal monazite can be identified from the mineral morphology, mineral paragenetic association and geochemical characteristics: e.g., the grain size is smaller than that of magmatic origin, and crystals often cluster in the form of granular geometry, are associated with sulfides and oxides and have lower contents of trace elements Th (<1%), Y, U, Sc, Sm and Gd and Th/U ratios but are enriched in light rare-earth elements such as La, Ce, Eu and Tb [93–95]. Monazite crystals from sample T29-10 of Cu-bearing carbonate veins are typically intergrown with hydrothermal mineral assemblages, including chalcopyrite, pyrite, carbonate, quartz and sericite with sizes of 10–50 μm (Figure 8i), indicating that the crystallization of monazite was coeval with copper deposition from the ore-forming fluid. Furthermore, partial trace element data in Table 3 display low Th (2–378 ppm), U (209–912 ppm) and Th/U (0–1.35) ratios, which also supports a typical hydrothermal origin.

Rutile is the common titanium dioxide polymorph as an accessory mineral, is widely distributed in metamorphic, igneous and sedimentary rocks and occurs in almost all deposits [29,88]. Rutile is also an “indicator” form and is preserved in many hydrothermal and metamorphic environments [88]. Although the main formula of rutile is TiO_2 , there are several possible element substitutions for titanium, including Al, V, Cr, Fe, Nb, Ta, Zr, Hf, Sn, Sb, W and U [96–99]. The change in the geochemical composition of the TiO_2 is dependent on the polymorph, the host rock and the hydrothermal fluids, which can trace the source of rutile and characterize the chemical and physical properties of rutile during its formation [29,88,97,100–107]: e.g., rutile from metallic hydrothermal deposits is usually characterized by high abundances of W, V, Sr, Cu, Sn and Sb, which can be

used to distinguish hydrothermal rutile crystals from those in igneous and metamorphic rocks [88,103,104]. In the BSE images, rutile grains in the sulfide-bearing quartz veins from the Tongmugou and Laobaotan deposits display bright–dark patchy zoning (Figure 6f–h), which may be mainly caused by high W anomalies or perhaps related to variations in Fe and Nb, based on the fact that the extremely small inclusions in the bright zones are CaWO_4 . The data in Table 2 show that the bright zones are more enriched in WO_3 (1.24–5.20 wt%), FeO (0.63–1.65 wt%), Nb_2O_5 (0.15–2.66 wt%) and V_2O_3 (0.46–1.21) than the dark zones. The high W abundance in rutile crystals may suggest the participation of hydrothermal fluids in the process of precipitation [88]. The high concentration of V in rutile grains is a favorable indicator of a hydrothermal origin [103]. More importantly, depending on the mineral assemblage, the rutile grains in the veins occur in association with sulfides such as chalcopyrite and pyrite, indicating that rutile precipitated simultaneously with copper mineralization in the hydrothermal veins. In summary, according to mineralogical and geochemical characteristics, both monazite and rutile are believed to have crystallized in a hydrothermal fluid system and to be closely related to copper mineralization. Therefore, monazite and rutile are of hydrothermal origin, and their nearly identical U–Pb isotope age of ca. 1850 Ma directly reflects the timing of stage II metamorphic hydrothermal copper mineralization.

5.2. Geochronology of Mineralization and Comment

Geochronological studies in the Hubi copper (cobalt) ore district from the Zhongtiao Mountain area have involved a variety of methods over recent decades (Table 6), including uraninite U–Pb, whole-rock Rb–Sr, molybdenite Re–Os and chalcopyrite Re–Os (Figure 13), which offer controversial interpretations and make it difficult to understand the SSC deposit model.

Table 6. Previous studies of age in Hubi copper deposits.

Age	Method	Sample and Occurrence	Deposit	Reference
1830 ± 34 Ma	Uraninite and brannerite U–Pb	Disseminated ore vein/Zhongtiao Group	Bizigou	[26]
1832 ± 26 Ma	Rb–Sr isochron	Carbonaceous schist	Nanhegou	[66]
		Quartz albitite	Nanhegou	
		Quartz albitite	Laobaotan	
		Quartz marble	Tongmugou	
1919~1980 Ma	Molybdenite Re–Os	Unknown	Bizigou	[108]
1901 ± 24 Ma	Molybdenite Re–Os	Molybdenite along faults and interlayer fracture zones, the relation with mineralization is unknown	Tongmugou	[27]
1952 ± 39 Ma	Chalcopyrite Re–Os	Chalcopyrite-bearing thick veins, stage II	Nanhegou	[28]
1577 ± 31 Ma	Molybdenite Re–Os	Molybdenite sulfide-bearing quartz veins	Bizigou	[109]

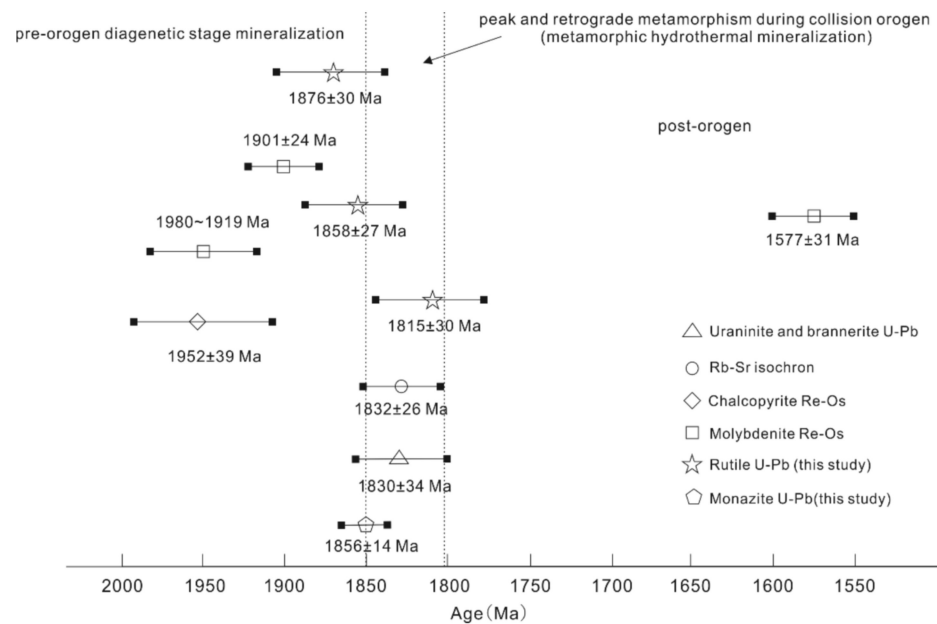


Figure 13. Compilation of geochronological data for the Hubi copper (cobalt) ore district. The data of the age are from [26–28,66,108,109].

The author of [26] was the first to obtain an age of 1830 ± 34 Ma by U-Pb dating of uraninite and brannerite from Zhongtiao Group strata in the Bizigou copper deposit and inferred that these U-bearing minerals are associated with mineralization, suggesting that the age represents the timing of copper mineralization. The age is consistent within error with the results from rutile and monazite in this study. On the one hand, the excessive U content may cause the U-Pb age to be lower than the actual mineralization age; on the other hand, the occurrence of the measured object is sparse, which may create confusion. Therefore, such ages may be difficult to interpret [28,105].

Subsequently, [66] conducted whole-rock Rb-Sr isochron dating for the host rocks of the Nanhegou, Laobaotan and Tongmugou copper deposits and obtained an isochron age of 1832 ± 26 Ma, which is considered the metallogenic age and close to the results in this study.

Molybdenite Re-Os dating is one of the few reliable methods to directly determine the timing of mineralization. Three previously published molybdenite Re-Os ages of 1919–1980 Ma, 1901 ± 24 Ma and 1577 ± 31 Ma represent different viewpoints and explanations [27,108]. However, the following problems have emerged: 1. Unavailable descriptions of the samples and occurrences lead to meaningless ages [108]. 2. A potential cogenetic association between molybdenum and copper within the ore-forming fluids is still ambiguous in the Hubi copper (cobalt) deposits: e.g., molybdenite occurred along faults and interlayer fracture zones [27], which makes the interpretation of molybdenite Re-Os ages uncertain; thus, they may not represent the timing of copper mineralization. 3. The gap in age results is too large, i.e., 1577 ± 31 Ma [109] to ca. 1900 Ma, and indicates a long age span (~330 myr), implying additional mineralization events. In summary, molybdenite Re-Os ages remain controversial and difficult to determine.

Recently, [28] performed Re-Os dating of chalcopyrite in Cu-bearing quartz veins (stage II) from the Nanhegou deposit in the Hubi ore district and reported an isochron age of 1932 ± 140 Ma and a mean model age of 1952 ± 39 Ma, representing the age of vein-like copper mineralization in the Nanhegou copper deposit and considered to be contemporaneous with regional metamorphism. However, the effectiveness of the chalcopyrite Re-Os system, especially closure, needs to be considered. At present, there are relatively few theoretical studies on the closure temperature of the sulfide Re-Os isotope system [110]. Due to the lack of support from experimental thermodynamic data, the closure temperature of the chalcopyrite Re-Os isotope system is still unclear,

and the sealing temperature of chalcopyrite and bornite is estimated to be greater than approximately 300 °C [111–113]. Note that the Zhongtiao Mountain area was generally affected by regional metamorphism of the greenschist facies to amphibolite facies, and the metamorphic temperature spans approximately 350–600 °C [36,68,69,114]. In addition, the fluid inclusion data also indicate that the temperature of the ore-forming fluid (stage II) was approximately 240–480 °C [80]. Moreover, if chalcopyrite and molybdenite coexist, the ^{187}Os in the molybdenite will enter the chalcopyrite by surface adsorption or diffusion, which also causes the chalcopyrite Re-Os isotope system to reset [115]. However, through the results of the age, old Re-Os ages of >ca. 1.9 Ga do not seem to have been reset.

The U-Pb dating of monazite and rutile can strongly resist resetting due to their high closure temperatures exceeding 700 °C and 500 °C [29,31,33,35,95,116], respectively, which are generally higher than most metamorphic and hydrothermal events; thus, this system has become a stable and reliable dating method for ore deposits. As mentioned above, it is convincingly proven that monazite and rutile are hydrothermal products from the aspects of mineral structure, paragenetic association of minerals and geochemical characteristics. Meanwhile, the LA-ICP-MS U-Pb isotope ages of hydrothermal monazite (1856 ± 14 Ma) and rutile (1858 ± 27 Ma) are consistent within error, also confirming the accuracy of the test results in this paper. Therefore, the new geochronological data directly represent the timing of the metamorphic hydrothermal copper mineralization event at ca. 1.85 Ga in the Hubi copper (cobalt) deposits.

5.3. Implication for Genesis and Metallogeny in Zhongtiao Mountain

The absolute ages of various ore deposits provide important constraints on the feasibility of genetic models and the coupling of geological events. However, in the case of sediment-hosted stratiform copper deposits, there is a general lack of ore-related minerals that are suitable for reliable isotope dating systems currently in use [17]. Among the global sediment-hosted stratiform copper deposits, the method of dating U-bearing accessory minerals has become widely accepted. A rutile U-Pb concordia age of 514 ± 2 Ma for ore-bearing veins supports post-peak metamorphic (during the Lufilian orogeny) mineralization in the Musoshi deposit, Zambian Copperbelt [34], which is also supported by monazite U-Th-Pb ages of 537.1 ± 6.6 Ma to 502.8 ± 6.3 Ma [117]. The dating of xenotime and monazite in Spar Lake red bed-associated Cu-Ag deposits indicates that mineralization occurred during late diagenesis [32]. The U-Pb ages of titanite-associated Cu from the large Udokan sediment-hosted stratiform Cu-Ag deposit in Russia imply that mineralization coincided with orogeny and metamorphism [7].

There is a broad consensus that the Trans-North China Orogen represents a collisional belt forming a suture between the Eastern and Western Blocks [40,41,46–61]. Regarding the evolution of the Neoproterozoic to Paleoproterozoic tectonic setting of the Trans-North China Orogen, [40,46,77,118] proposed the following points. (1) At ca. 2.56 Ga, the Wutai and Lüliang Complexes, including the Zhongtiao Complex, were part of an active continental margin arc developed on the western margin of the Eastern Block, which was separated from the Western Block by an old ocean. Subsequently, the oceanic lithosphere continuously subducted under the Eastern Block at a high angle to form a series of TTG rocks. (2) At ca. 2.1 Ga, due to the continuous subduction of the Western Block beneath the Eastern Block, a back-arc basin system developed by extension behind the active continental margin magmatic arc. The Jiangxian Group and Zhongtiao Group (and other shallow metamorphosed supercrustal rocks in the Trans-North China Orogen) were formed here [41,63,77,119–124], and greenschist facies metamorphism occurred during the subsequent collisional orogeny. (3) At ca. 1.85 Ga, the continental collision of the Eastern and Western Blocks began, which resulted in significant crustal thickening, the formation of a foreland basin and the deposition of siliceous clastic rocks mainly composed of molasse formations, namely, the Danshanshi Group. Meanwhile, the ages of tectonic thermal events in the Trans-North China Orogen indicate that deformation related to crustal thickening occurred from 1843 to 1817 Ma [125], the peak and retrograde metamorphism ages were

limited from 1849 to 1814 Ma [42,52,57,58,65,126] and the emplacement time of syncollisional granites was ca. 1832 Ma [118]. Therefore, the new data presented in this paper are consistent with the age of peak and retrograde metamorphism caused by the collisional orogeny at ca. 1.85 Ga.

Traditionally, two stages of mineralization are considered to have occurred in the Hubi copper (cobalt) ore district: the early sedimentary diagenetic stage and the late hydrothermal stage. Although the Hubi copper (cobalt) ore district was transformed by metamorphism and has characteristics of a metamorphic origin, the sedimentary conditions were the dominant controlling factors of mineralization in previous detailed studies [2,80,127]. Similar to the situation in the Zambian Copperbelt, an earlier pre-Lufilian mineralization event cannot be ignored based on evidence from decades of careful geological work [22,25]. Consequently, the primary sedimentary mineralization of the Hubi copper (cobalt) ore district was synchronous with the deposition of the Zhongtiao Group at ca. 2168 Ma to ca. 2059 Ma, as mentioned above, despite the absence of direct dating data. The subsequent synorogenic metamorphic hydrothermal mineralization age can be confirmed as 1850 Ma. From the perspective of mineralization age, the typical SSC-type deposits in both the Zambian Copperbelt and the Hubi copper (cobalt) ore district experienced early preorogenic sedimentary diagenetic mineralization and late metamorphic hydrothermal mineralization related to orogenesis, i.e., the Trans-North China Orogen and the Lufilian Orogen, respectively [10,17,21,22,25]. Moreover, the Hubi copper (cobalt) deposits are the oldest SSC-type deposits in China and even in the world and are equivalent to the Udokan deposit in Russia [18].

In our research, we also found an interesting metallogenic regularity; that is, all the different types of copper deposits in the Zhongtiao Mountain ore area developed during almost the same stage of metamorphic hydrothermal mineralization. A recent study by [38] confirmed that the Tongkuangyu porphyry deposit experienced the original porphyry copper mineralization at ca. 2.1 Ga, followed by metamorphic hydrothermal remobilization of copper during the orogeny at ca. 1.8 Ga through U-Pb dating of hydrothermal monazite (1832 ± 16 Ma, 1810 ± 14 Ma and 1809 ± 12 Ma) and Re-Os dating of pyrite (1807 ± 4 Ma). The authors of [36] dated the monazite of mineralization veins in the Henglingguan deposit and obtained a U-Pb age of 1863 ± 17 Ma, indicating that Cu mineralization formed during the retrograde cooling stage related to the postorogenic stage. Moreover, within the widely exposed mafic dikes that intruded into the Zhongtiao Group, abundant Cu-bearing quartz dolomite veins developed. Ar-Ar dating of muscovite associated with chalcopyrite in the veins shows a plateau age of 1857.9 ± 14.2 Ma and an isochron age of 1859.7 ± 14.5 Ma (unpublished), representing the timing of thermal events and copper mineralization. The above data indicate that the influence of metamorphic hydrothermal events is extremely large, not only transforming the original mineralization of various types of deposits in the ore area but also causing remobilization of mafic dikes with a certain concentration of copper, leading to copper precipitation in hydrothermal veins. In summary, mineralization ages of ~ 1.80 Ga to ~ 1.85 Ga are of great significance to interpret the genesis and prospecting of the deposits.

6. Conclusions

Rutile and monazite crystals are common accessory minerals that have a paragenetic association with copper mineralization in Cu-bearing quartz veins of the Tongmugou and Laobaotan deposits from the Zhongtiao Mountain area. Mineralogical and geochemical characteristics suggest that both rutile and monazite are hydrothermal in origin. LA-ICP-MS dating of the rutile grains yielded U-Pb ages of 1815 ± 30 Ma and 1858 ± 27 Ma for Tongmugou and 1876 ± 30 Ma for Laobaotan. Meanwhile, monazite from Tongmugou shows a weighted mean $^{207}\text{Pb}/^{206}\text{Pb}$ age of 1856 ± 14 Ma, which is close to that of rutile within error. The new age data directly represent the timing of metamorphic hydrothermal copper mineralization at ca. 1.85 Ga in Tongmugou and Laobaotan, also known as the Hubi copper (cobalt) ore district. These data confirm that this precise age is consistent with

that of peak and retrograde metamorphism caused by a collision of the Trans-North China Orogen at ca. 1.85 Ga, and the Hubi copper (cobalt) ore district could be the oldest SSC-type deposit in China and even in the world. Moreover, this mineralization event affected a wide range in the Zhongtiao Mountain region and has great significance.

Author Contributions: Conceptualization, M.W. and J.M.; methodology, M.W.; software, M.W.; validation, M.W., J.M. and H.Y.; formal analysis, M.W.; investigation, M.W.; resources, H.Y.; data curation, M.W.; writing—original draft preparation, M.W.; writing—review and editing, J.M.; visualization, M.W.; supervision, H.L.; project administration, H.Y.; funding acquisition, H.L. All authors have read and agreed to the published version of the manuscript.

Funding: This research was funded by the Geological Survey Project of China (DD20160124).

Data Availability Statement: The data used to support the findings of this study are available from the corresponding author upon request.

Conflicts of Interest: The authors declare no conflict of interest.

References

1. Pang, X.J. Study on the Enrichment Regularities and the Ore Genetic Rules of Nanhegou and Laobaotan Copper Deposits in Zhongtiao Mountains, Shanxi Province. Master's Thesis, JiLin University, Changchun, China, 2010; pp. 60–71. (In Chinese).
2. Zhang, H. Metallogenesis of Paleoproterozoic Copper Deposits in the Northern Zhongtiao Mountains, Shanxi Province. Ph.D. Thesis, JiLin University, Changchun, China, 2012; pp. 119–123. (In Chinese).
3. Boyle, R.W.; Brown, A.C.; Jefferson, C.W.; Jowett, E.C. Sediment-hosted stratiform copper deposits. *Geosci. Can.* **1992**, *19*, 125–139.
4. Hitzman, M.W.; Kirkham, R.; Broughton, D.; Thorson, J.; Selley, D. The Sediment-Hosted Stratiform Copper Ore System. In *Geology 100th Anniversary Volume*; Society of Economic Geologists: Littleton, CO, USA, 2005; pp. 609–642.
5. Sillitoe, R.H. *Copper Provinces*; Special Publication; Society of Economic Geologists: Littleton, CO, USA, 2012; Volume 16, pp. 1–18.
6. Volodin, R.N.; Chechetkin, V.S.; Bogdanov, Y.V.; Narkelyun, L.F.; Trubachev, A.I. The Udokan cupriferous sandstones deposit (eastern Siberia). *Geol. Ore Depos.* **1994**, *36*, 1–25.
7. Perelló, J.; Sillitoe, R.H. Age and tectonic setting of the Udokan sediment-hosted copper-silver deposit, Transbaikalia, Russia. *Ore Geol. Rev.* **2017**, *86*, 856–866. [[CrossRef](#)]
8. Sawlowicz, Z. REE and their relevance to the development of the Kupferschiefer copper deposit in Poland. *Ore Geol. Rev.* **2013**, *55*, 176–186. [[CrossRef](#)]
9. Brown, A.C. World-class sediment-hosted stratiform copper deposits: Characteristics, genetic concepts and metallogenesis. *Austr. J. Earth Sci.* **1997**, *44*, 317–328. [[CrossRef](#)]
10. Selley, D.; Broughton, D.; Scott, R.; Hitzman, M.; Bull, S.; Large, R.; McGoldrick, P.; Croaker, M.; Pollington, N.; Barra, F. A New Look at the Geology of the Zambian Copperbelt. In *Economic Geology 100th Anniversary Volume*; Hedenquist, J.W., Thompson, J.F.H., Goldfarb, R.J., Richards, J.P., Eds.; Society of Economic Geologists: Littleton, CO, USA, 2005; pp. 965–1000.
11. Hitzman, M.W.; Selley, D.; Bull, S. Formation of sedimentary rock-hosted stratiform copper deposits through Earth history. *Econ. Geol.* **2010**, *105*, 627–639. [[CrossRef](#)]
12. Cailteux, J.; Binda, P.; Katekesha, W.M.; Kampunzu, A.B.; Intiomale, M.M.; Kapenda, D.; Kaunda, C.; Ngongo, K.; Tshiauka, T.; Wendorff, M. Lithostratigraphic correlation of the Neoproterozoic Roan Supergroup from Shaba (Zaire) and Zambia, in the central African copper-cobalt metallogenic province. *J. Afr. Earth Sci.* **1994**, *19*, 265–278. [[CrossRef](#)]
13. Kampunzu, A.B.; Cailteux, J. Tectonic evolution of the Lufilian arc (Central Africa Copper Belt) during Neoproterozoic Pan African orogenesis. *Gondwana Res.* **1999**, *2*, 401–421. [[CrossRef](#)]
14. McGowan, R.R.; Roberts, S.; Foster, R.P.; Boyce, A.J.; Coller, D. Origin of the copper-cobalt deposits of the Zambian Copperbelt: An epigenetic view from Nchanga. *Geology* **2003**, *31*, 497–500. [[CrossRef](#)]
15. Sillitoe, R.H.; Perelló, J.; García, A. Sulfide-bearing veinlets throughout the stratiform mineralization of the Central African Copperbelt: Temporal and genetic implications. *Econ. Geol.* **2010**, *105*, 1361–1368. [[CrossRef](#)]
16. Sillitoe, R.H.; Perelló, J.; Creaser, R.A.; Wilton, J.; Dawborn, T. Two ages of copper mineralization in the Mwombezhi dome, northwestern Zambia: Metallogenic implications for the Central African Copperbelt. *Econ. Geol.* **2015**, *110*, 1917–1923. [[CrossRef](#)]
17. Sillitoe, R.H.; Perelló, J. Age of the Zambian Copperbelt. *Miner. Depos.* **2017**, *52*, 1245–1268. [[CrossRef](#)]
18. Perelló, J.; Clifford, J.A.; Creaser, R.A.; Valencia, V.A. An example of synorogenic sediment-hosted copper mineralization: Geologic and geochronologic evidence from the Paleoproterozoic Nussir deposit, Finnmark, Arctic Norway. *Econ. Geol.* **2015**, *110*, 677–689. [[CrossRef](#)]
19. El Desouky, H.A.; Muchez, P.; Cailteux, J. Two Cu-Co phases and contrasting fluid systems in the Katanga Copperbelt, Democratic Republic of Congo. *Ore Geol. Rev.* **2009**, *36*, 315–332. [[CrossRef](#)]
20. El Desouky, H.A.; Muchez, P.; Boyce, A.J.; Schneider, J.; Cailteux, J.L.H.; Dewaele, S.; von Quadt, A. Genesis of sediment-hosted stratiform Cu-Co mineralization at Luiswishi and Kamoto, Katanga Copperbelt (Democratic Republic of Congo). *Miner. Depos.* **2010**, *45*, 735–763. [[CrossRef](#)]

21. Hitzman, M.W.; Broughton, D.; Selley, D.; Woodhead, J.; Wood, D.; Bull, S. The Central African Copperbelt: Diverse Stratigraphic, Structural, and Temporal Settings in the World's Largest Sedimentary Copper District. In *Geology and Genesis of Major Copper Deposits and Districts of the World: A Tribute to Richard, H. Sillitoe*; Special Publications of the Society of Economic Geologists; Hedenquist, J.W., Harris, M., Camus, F., Eds.; Society of Economic Geologists: Littleton, CO, USA, 2012; Volume 16, pp. 487–514.
22. Hitzman, M.W.; Broughton, D. Discussion: "Age of the Zambian Copperbelt" by Sillitoe et al. *Miner. Depos.* **2017**, *52*, 1273–1275. [[CrossRef](#)]
23. Muchez, P.; Brems, D.; Clara, E.; De Cleyn, A.; Lammens, L.; Boyce, A.; De Muynck, D.; Mukumba, W.; Sikazwe, O. Evolution of Cu–Co mineralizing fluids at Nkana Mine, Central African Copperbelt, Zambia. *J. Afr. Earth Sci.* **2010**, *58*, 457–474. [[CrossRef](#)]
24. Muchez, P.; André-Mayer, A.-S.; El Desouky, E.L.; Reisberg, L. Diagenetic origin of the stratiform Cu-Co deposit at Kamoto in the Central African Copperbelt. *Miner. Depos.* **2015**, *50*, 437–447. [[CrossRef](#)]
25. Muchez, P.; André-Mayer, A.-S. Discussion: Age of the Zambian Copperbelt. *Miner. Depos.* **2017**, *52*, 1269–1271. [[CrossRef](#)]
26. Tao, Q. *Geological Ages of Precambrian Strata in the Zhongtiao Mountains*; Tianjin Institute of Geology and Mineral Resources, C.A.G.S.: Tianjin, China; Geological Publishing House: Beijing, China, 1985. (In Chinese)
27. Zhang, L.; Li, B.L.; Zhang, H.; Hu, A.X. Re-Os isotopic dating and its geological significance of molybdenite, from Tongmugou copper deposit in Zhongtiaoshan, Shanxi. *Glob. Geol.* **2013**, *32*, 740–746. (In Chinese)
28. Qiu, Z.J.; Fan, H.R.; Liu, X. Mineralogy, chalcopyrite Re-Os geochronology and sulfur isotope of the Hujiayu Cu deposit in the Zhongtiao Mountains, North China Craton: Implications for a Paleoproterozoic metamorphogenic copper mineralization. *Ore Geol. Rev.* **2016**, *78*, 252–267. [[CrossRef](#)]
29. Meinhold, G. Rutile and its applications in earth sciences. *Earth-Sci. Rev.* **2010**, *102*, 1–28. [[CrossRef](#)]
30. Li, N.; Chen, Y.J.; Fletcher, I.R.; Zeng, Q.T. Triassic mineralization with Cretaceous overprint in the Dahu Au-Mo deposit, Xiaoqinling gold province: Constraints from SHRIMP monazite U-Th-Pb geochronology. *Gondwana Res.* **2011**, *20*, 543–552. [[CrossRef](#)]
31. Zack, T.; Stockli, D.F.; Luvizotto, G.L.; Barth, M.G.; Belousova, E.; Wolfe, M.R.; Hinton, R.W. In situ U-Pb rutile dating by LA-ICP-MS: 208Pb correction and prospects for geological applications. *Contrib. Mineral. Petrol.* **2011**, *162*, 515–530. [[CrossRef](#)]
32. Aleinikoff, J.N.; Hayes, T.S.; Evans, K.V.; Mazdab, F.K.; Pillers, R.M.; Fanning, C.M. SHRIMP U-Pb ages of xenotime and monazite from the Spar Lake red bed-associated Cu-Ag deposit, western Montana: Implications for ore genesis. *Econ. Geol.* **2012**, *107*, 1251–1274. [[CrossRef](#)]
33. Zack, T.; Kooijman, E. Petrology and geochronology of rutile. *Rev. Mineral. Geochem.* **2017**, *83*, 443–467. [[CrossRef](#)]
34. Richards, J.P.; Krogh, T.E.; Spooner, E.T.C. Fluid inclusion characteristics and U-Pb rutile age of late hydrothermal alteration and veining at the Musoshi stratiform copper deposit, Central African Copper Belt, Zaire. *Econ. Geol.* **1988**, *83*, 118–139. [[CrossRef](#)]
35. Pi, Q.H.; Hu, R.Z.; Xiong, B.; Li, Q.L.; Zhong, R.C. In situ SIMS U-Pb dating of hydrothermal rutile: Reliable age for the Zhesang Carlin-type gold deposit in the golden triangle region, SW China. *Miner. Depos.* **2017**, *52*, 1179–1190. [[CrossRef](#)]
36. Qiu, Z.J.; Fan, H.R.; Liu, X. Metamorphic P-T-t evolution of Paleoproterozoic schist-hosted Cu deposits in the Zhongtiao Mountains, North China Craton: Retrograde ore formation during sluggish exhumation. *Precambrian Res.* **2017**, *300*, 59–77. [[CrossRef](#)]
37. Fielding, I.O.H.; Johnson, S.P.; Zi, J.-W.; Rasmussen, B.; Muhling, J.R.; Dunkley, D.J.; Sheppard, S.; Wingate, M.T.D.; Rogers, J.R. Using in situ SHRIMP U-Pb monazite and xenotime geochronology to determine the age of orogenic gold mineralization: An example from the Paulsens mine, southern Pilbara craton. *Econ. Geol.* **2017**, *112*, 1205–1230. [[CrossRef](#)]
38. Meng, X.Y.; Richards, J.; Mao, J.W. The Tongkuangyu Cu Deposit, Trans-North China Orogen: A Metamorphosed Paleoproterozoic Porphyry Cu Deposit. *Econ. Geol.* **2020**, *115*, 51–77. [[CrossRef](#)]
39. Liu, J.C.; Wang, Y.T.; Mao, J.W. Precise ages for lode gold mineralization in the Xiaoqinling gold field, Southern margin of the North China Craton: New constraints from in situ U-Pb dating of hydrothermal monazite and rutile. *Econ. Geol.* **2021**, *116*, 773–786. [[CrossRef](#)]
40. Zhao, G.C.; Sun, M.; Wilde, S.A.; Li, S.Z. Late Archean to Paleoproterozoic evolution of the North China Craton: Key issues revisited. *Precambrian Res.* **2005**, *136*, 177–202. [[CrossRef](#)]
41. Zhao, G.C.; Wilde, S.A.; Cawood, P.A.; Sun, M. Archean blocks and their boundaries in the North China Craton: Lithological, geochemical, structural and P-T path constraints and tectonic evolution. *Precambrian Res.* **2001**, *107*, 45–73. [[CrossRef](#)]
42. Zhao, G.C.; Wilde, S.A.; Cawood, P.A.; Sun, M. SHRIMP U-Pb zircon ages of the Fuping Complex: Implications for late Archean to Paleoproterozoic accretion and assembly of the North China Craton. *Am. J. Sci.* **2002**, *302*, 191–226. [[CrossRef](#)]
43. Zhai, M.G. Tectonic evolution and metallogenesis of North China Craton. *Miner. Depos.* **2010**, *29*, 24–36. (In Chinese)
44. Zhai, M.G.; Peng, P. Paleoproterozoic events in the North China Craton. *Acta Petrol. Sin.* **2007**, *23*, 2665–2682. (In Chinese)
45. Zhai, M.G.; Santosh, M. The early Precambrian odyssey of the North China Craton: A synoptic overview. *Gondwana Res.* **2011**, *20*, 6–25. [[CrossRef](#)]
46. Zhao, G.C.; Cawood, P.A.; Wilde, S.A.; Sun, M.; Lu, L.Z. Metamorphism of basement rocks in the Central Zone of the North China Craton: Implications for Paleoproterozoic tectonic evolution. *Precambrian Res.* **2000**, *103*, 55–88. [[CrossRef](#)]
47. Guo, J.H.; O'Brien, P.J.; Zhai, M.G. High-pressure granulites in the Sanggan area, North China Craton: Metamorphic evolution, P-T paths and geotectonic significance. *J. Metamorph. Geol.* **2002**, *20*, 741–756. [[CrossRef](#)]

48. Guo, J.H.; Sun, M.; Chen, F.K.; Zhai, M.G. Sm-Nd and SHRIMP UPb zircon geochronology of high-pressure granulites in the Sanggan area, North China Craton: Timing of Paleoproterozoic continental collision. *J. Asian Earth Sci.* **2005**, *24*, 629–642. [[CrossRef](#)]
49. Liu, S.W.; Pan, Y.M.; Li, J.H.; Li, Q.G.; Zhang, J. Geological and isotopic geochemical constraints on the evolution of the Fuping Complex, North China Craton. *Precambrian Res.* **2002**, *117*, 41–56. [[CrossRef](#)]
50. Liu, S.W.; Pan, Y.M.; Xie, Q.L.; Zhang, J.; Li, Q.G. Archean geodynamics in the Central Zone, North China Craton: Constraints from geochemistry of two contrasting series of granitoids in the Fuping and Wutai complexes. *Precambrian Res.* **2004**, *130*, 229–249. [[CrossRef](#)]
51. Liu, S.W.; Pan, Y.M.; Xie, Q.L.; Zhang, J.; Li, Q.G.; Yang, B. Geochemistry of the Paleoproterozoic Nanying granitic gneisses in the Fuping Complex: Implications for the tectonic evolution of the Central Zone, North China Craton. *J. Asian Earth Sci.* **2005**, *24*, 643–658. [[CrossRef](#)]
52. Liu, S.W.; Zhao, G.C.; Wilde, S.A.; Shu, G.M.; Sun, M.; Li, Q.G.; Tian, W.; Zhang, J. Th-U-Pb monazite geochronology of the Luliang and Wutai complexes: Constraints on the tectonothermal evolution of the Trans-North China Orogen. *Precambrian Res.* **2006**, *148*, 205–224. [[CrossRef](#)]
53. Wilde, S.A.; Zhao, G.C.; Sun, M. Development of the North China Craton during the Late Archean and its final amalgamation at 1.8Ga: Some speculations on its position within a global Palaeoproterozoic supercontinent. *Gondwana Res.* **2002**, *5*, 85–94. [[CrossRef](#)]
54. Kusky, T.M.; Li, J.H. Paleoproterozoic tectonic evolution of the North China Craton. *J. Asian Earth Sci.* **2003**, *22*, 383–397. [[CrossRef](#)]
55. Wang, Y.J.; Fan, W.M.; Zhang, Y.H.; Guo, F.; Zhang, H.F.; Peng, T.P. Geochemical $^{40}\text{Ar}/^{39}\text{Ar}$ geochronological and Sr-Nd isotopic constraints on the origin of Paleoproterozoic mafic dikes from the southern Taihang Mountains and implications for the ca.1800Ma event of the North China Craton. *Precambrian Res.* **2004**, *135*, 55–77. [[CrossRef](#)]
56. Wang, Y.J.; Zhao, G.C.; Fan, W.M.; Peng, T.P.; Sun, L.H.; Xia, X.P. LA-ICP-MS U-Pb zircon geochronology and geochemistry of Paleoproterozoic mafic dykes from western Shandong Province: Implications for back-arc basin magmatism in the Eastern Block, North China Craton. *Precambrian Res.* **2007**, *154*, 107–124. [[CrossRef](#)]
57. Kröner, A.; Wilde, S.A.; Li, J.H.; Wang, K.Y. Age and evolution of a Late Archean to Paleoproterozoic upper to lower crustal section in the Wutaishan/Hengshan/Fuping terrain of northern China. *J. Asian Earth Sci.* **2005**, *24*, 577–595. [[CrossRef](#)]
58. Kröner, A.; Wilde, S.A.; Zhao, G.C.; O'Brien, P.J.; Sun, M.; Liu, D.Y.; Wan, Y.S.; Liu, S.W.; Guo, J.H. Zircon geochronology and metamorphic evolution of mafic dykes in the Hengshan Complex of northern China: Evidence for late Palaeoproterozoic extension and subsequent high-pressure metamorphism in the North China Craton. *Precambrian Res.* **2006**, *146*, 45–67. [[CrossRef](#)]
59. Wilde, S.A.; Zhao, G.C. Archean to Paleoproterozoic evolution of the North China Craton. *J. Asian Earth Sci.* **2005**, *24*, 519–522. [[CrossRef](#)]
60. Wu, F.Y.; Zhao, G.C.; Wilde, S.A.; Sun, D.Y. Nd isotopic constraints on crustal formation in the North China Craton. *J. Asian Earth Sci.* **2005**, *24*, 523–545. [[CrossRef](#)]
61. Li, J.H.; Kusky, T.M. A Late Archean foreland fold and thrust belt in the North China Craton: Implications for early collisional tectonics. *Gondwana Res.* **2007**, *12*, 47–66. [[CrossRef](#)]
62. Zhang, J.; Zhao, G.C.; Li, S.Z.; Sun, M.; Liu, S.W.; Wilde, S.A.; Kröner, A.; Yin, C.Q. Deformation history of the Hengshan Complex: Implications for the tectonic evolution of the Trans-North China Orogen. *J. Struct. Geol.* **2007**, *29*, 933–949. [[CrossRef](#)]
63. Trap, P.; Faure, M.; Lin, W.; Monie, P. Late Paleoproterozoic (1900–1800Ma) nappe stacking and polyphase deformation in the Hengshan-Wutaishan area: Implications for the understanding of the Trans-North-China belt, North China Craton. *Precambrian Res.* **2007**, *156*, 85–106. [[CrossRef](#)]
64. Trap, P.; Faure, M.; Lin, W.; Bruguier, O.; Monie, P. Contrasted tectonic styles for the Paleoproterozoic evolution of the North China Craton: Evidence for a similar to 2.1Ga thermal and tectonic event in the Fuping Massif. *J. Struct. Geol.* **2008**, *30*, 1109–1125. [[CrossRef](#)]
65. Wang, J.; Wu, Y.B.; Gao, S.; Peng, M.; Liu, X.C.; Zhao, L.S.; Zhou, L.; Hu, Z.C.; Gong, H.Z.; Liu, Y.S. Zircon U-Pb and trace element data from rocks of the Huai'an Complex: New insights into the Late Paleoproterozoic collision between the Eastern and Western blocks of the North China Craton. *Precambrian Res.* **2010**, *178*, 59–71. [[CrossRef](#)]
66. Sun, D.Z.; Hu, W.X.; Tang, M.; Zhao, F.Q.; Condie, K.C. Origin of Late Archean and Early Proterozoic rocks and associated mineral deposits from the Zhongtiao Mountains, east-central China. *Precambrian Res.* **1990**, *47*, 287–306.
67. Sun, D.Z.; Li, H.M.; Lin, Y.X.; Zhou, H.F.; Zhao, F.Q.; Tang, M. Precambrian geochronology, chronotectonic framework and model of chronocrustal structure of the Zhongtiao Mountains. *Acta Geol. Sin. Engl. Ed.* **1992**, *5*, 23–37.
68. Sun, D.Z.; Hu, W.X. *Precambrian Geochronology, Chronotectonic Framework and Model of Chronocrustal Structure of the Zhongtiao Mountains*, 1st ed.; Geological Publishing House: Beijing, China, 1993; pp. 1–102. (In Chinese)
69. Bai, J. Precambrian crustal evolution of the Zhongtiao Mountains. *Earth Sci. Front.* **1997**, *4*, 281–289. (In Chinese)
70. Zhu, M.T.; Zhang, L.C.; Wu, G.; He, H.Y.; Cui, M.L. Fluid inclusions and He Ar isotopes in pyrite from the Yinjiagou deposit in the southern margin of the North China Craton: A mantle connection for poly-metallic mineralization. *Chem. Geol.* **2013**, *351*, 1–14. [[CrossRef](#)]
71. Zhang, R.Y. The composition and evolution of the Sushui complex in the Zhongtiao Mountains, the south of North China Craton. Ph.D. Thesis, Northwest University, Xi'an, China, 2015; pp. 15–26. (In Chinese).

72. Zhao, F.Q. Geochronologic and geochemical constraints on the Paleoproterozoic crustal evolution of Zhongtiao Mountains from Shanxi Province. Ph.D. Thesis, China University of Geosciences, Beijing, China, 2006; pp. 31–77. (In Chinese).
73. Li, Q.; Liu, S.; Wang, Z.; Zhang, F.; Chen, Y.; Wang, T. LA-ICP-MS U-Pb geochronology of the detrital zircons from the Jiangxian Group in the Zhongtiao Mountain and its tectonic significance. *Acta Petrol. Sin.* **2008**, *24*, 1359–1368. (In Chinese)
74. Liu, X.; Fan, H.R.; Santosh, M.; Yang, K.F.; Qiu, Z.J.; Hu, F.F.; Wen, B.J. Geological and geochronological constraints on the genesis of the giant Tongkuangyu Cu deposit (Palaeoproterozoic), North China Craton. *Int. Geol. Rev.* **2016**, *58*, 155–170. [[CrossRef](#)]
75. Liu, C.H.; Liu, F.L.; Zhao, G.C. The Paleoproterozoic basin evolution in the Trans-North China Orogen, North China Craton. *Acta Petrol. Sin.* **2012**, *28*, 2770–2784.
76. Liu, X.; Fan, H.R.; Qiu, Z.J.; Yang, K.F. Formation ages of the Jiangxian and Zhongtiao groups in the Zhongtiao Mountain region, North China Craton: Insights from SIMS U-Pb dating on zircons of intercalated plagioclase amphibolites. *Acta Petrol. Sin.* **2015**, *31*, 1564–1572.
77. Liu, C.H.; Zhao, G.C.; Sun, M.; Zhang, J.; Yin, C.Q. U-Pb geochronology and Hf isotope geochemistry of detrital zircons from the Zhongtiao Complex: Constraints on the tectonic evolution of the Trans-North China Orogen. *Precambrian Res.* **2012**, *222*–223, 159–172. [[CrossRef](#)]
78. Zhao, T.; Zhai, M.; Xia, B.; Li, H.; Zhang, Y.; Wan, Y. Zircon U-Pb SHRIMP dating for the volcanic rocks of the Xiong'er Group: Constraints on the initial formation age of the cover of the North China Craton. *Chin. Sci. Bull.* **2004**, *49*, 2495–2502. [[CrossRef](#)]
79. Hu, W.X.; Sun, D.Z. Mineralization and evolution of the Early Proterozoic copper deposits in the Zhongtiao Mountains. *Acta Geol. Sin. Engl. Ed.* **1987**, *61*, 152–166. (In Chinese)
80. Jiang, Y.; Niu, H.; Bao, Z.; Li, N.; Shan, Q.; Yang, W.; Yan, S. Fluid evolution of the Paleoproterozoic Hujiaayu copper deposit in the Zhongtiaoshan region: Evidence from fluid inclusions and carbon-oxygen isotopes. *Precambrian Res.* **2014**, *255*, 734–747. [[CrossRef](#)]
81. Luvizotto, G.L.; Zack, T. Nb and Zr behavior in rutile during high-grade metamorphism and retrogression: An example from the Ivrea-Verbano Zone. *Chem. Geol.* **2009**, *261*, 303–317. [[CrossRef](#)]
82. Bracciali, L.; Parrish, R.R.; Horstwood, M.S.A.; Condon, D.J.; Najman, Y. U-Pb LA-(MC)-ICP-MS dating of rutile: New reference materials and applications to sedimentary provenance. *Chem. Geol.* **2013**, *347*, 82–101. [[CrossRef](#)]
83. Liu, Y.S.; Hu, Z.C.; Zong, K.Q.; Gao, C.G.; Gao, S.; Xu, J.A.; Chen, H.H. Reappraisal and refinement of zircon U-Pb isotope and trace element analyses by LA-ICP-MS. *Chin. Sci. Bull.* **2010**, *55*, 1535–1546. [[CrossRef](#)]
84. Liu, Y.S.; Gao, S.; Hu, Z.C.; Gao, C.G.; Zong, K.Q.; Wang, D.B. Continental and oceanic crust recycling-induced melt-peridotite interactions in the Trans-North China orogen: U-Pb dating, Hf isotopes and trace elements in zircons from mantle xenoliths. *J. Petrol.* **2010**, *51*, 537–571. [[CrossRef](#)]
85. Ludwig, K.R. *User's Manual for Isoplot/Ex. Version 3.00: A Geochronological Toolkit for Microsoft Excel*; Special Publication 4; Berkeley Geochronology Center: Berkeley, CA, USA, 2003; pp. 1–77.
86. Porto, S.P.S.; Fleury, P.A.; Damen, T.C. Raman spectra of TiO₂, MgF₂, ZnF₂, FeF₂, and MnF₂. *Phys. Rev.* **1967**, *154*, 522–526. [[CrossRef](#)]
87. Tompsett, G.A.; Bowmaker, G.A.; Cooney, R.P.; Metson, J.B.; Rodgers, K.A.; Seakins, J.M. The Raman spectrum of brookite, TiO₂ (Pbc₂, Z = 8). *J. Raman Spectrosc.* **1995**, *26*, 57–62. [[CrossRef](#)]
88. Clark, J.R.; Williams-Jones, A.E. *Rutile as a Potential Indicator Mineral for Metamorphosed Metallic Ore Deposits*; Rapport Final de DIVEX, Sous-Projet SC2; McGill University: Montréal, QC, Canada, 2004; 17p.
89. Poitras, F.; Hanchar, J.M.; Schaltegger, U. The current state of accessory mineral research. *Chem. Geol.* **2001**, *191*, 3–24. [[CrossRef](#)]
90. DeWolf, C.P.; Belshaw, N.S.; O'Nions, R.K. A metamorphic history from micro-scale 207Pb-206Pb chronometry of Archean monazite. *Earth Planet. Sci. Lett.* **1993**, *120*, 207–220. [[CrossRef](#)]
91. Zhu, X.K.; O'Nions, R.K.; Belshaw, N.S.; Gibb, A.J. Lewisian crustal history from in situ SIMS mineral chronometry and related metamorphic textures. *Chem. Geol.* **1997**, *136*, 205–218. [[CrossRef](#)]
92. Bingen, B.; van Breeman, O. U-Pb monazite ages in amphibolite to granulite facies orthogneiss reflect hydrous mineral breakdown reaction: Sveconorwegian Province of SW Norway. *Contrib. Mineral Petrol.* **1998**, *132*, 336–353. [[CrossRef](#)]
93. Cocherie, A.; Legendre, O.; Peucat, J.J.; Kouamelan, A.N. Geochronology of polygenetic monazites constrained by in situ electron microprobe Th-U-total lead determination: Implications for lead behaviour in monazite. *Geochim. Cosmochim. Acta* **1998**, *62*, 2475–2497. [[CrossRef](#)]
94. Hong, W.X.; Zhu, X.K. A Microanalysis Study on Monazite Composition Distribution. *Geol. J. China Univ.* **2000**, *6*, 167–171. (In Chinese)
95. Schandl, E.S.; Gorton, M.P. A textural and geochemical guide to the identification of hydrothermal monazite criteria for selection of samples for dating epigenetic hydrothermal ore deposits. *Econ. Geol.* **2004**, *99*, 1027–1035. [[CrossRef](#)]
96. Rice, C.; Darke, K.; Still, J. Tungsten-bearing rutile from the Kori Kollo gold mine Bolivia. *Mineral. Mag.* **1998**, *62*, 421–429. [[CrossRef](#)]
97. Zack, T.; Kronz, A.; Foley, S.F.; Rivers, T. Trace element abundances in rutiles from eclogites and associated garnet mica schists. *Chem. Geol.* **2002**, *184*, 97–122. [[CrossRef](#)]
98. Bromiley, G.D.; Hilairet, N. Hydrogen and minor element incorporation in synthetic rutile. *Mineral. Mag.* **2005**, *69*, 345–358. [[CrossRef](#)]

99. Carruzzo, S.; Clarke, D.B.; Pelrine, K.M.; MacDonald, M.A. Texture, composition, and origin of rutile in the South Mountain Batholith, Nova Scotia. *Can. Mineral.* **2006**, *44*, 715–729. [[CrossRef](#)]
100. Rudnick, R.L.; Barth, M.; Horn, I.; McDonough, W.F. Rutile-bearing refractory eclogites: Missing link between continents and depleted mantle. *Science* **2000**, *287*, 278–281. [[CrossRef](#)]
101. Zack, T.; Moraes, R.; Kronz, A. Temperature dependence of Zr in rutile: Empirical calibration of a rutile thermometer. *Contr. Min. Petrol.* **2004**, *148*, 471–488. [[CrossRef](#)]
102. Zack, T.; von Eynatten, H.; Kronz, A. Rutile geochemistry and its potential use in quantitative provenance studies. *Sediment. Geol.* **2004**, *171*, 37–58. [[CrossRef](#)]
103. Scott, K.M. Rutile geochemistry as a guide to porphyry Cu–Au mineralization, Northparkes, New South Wales, Australia. *Geochem. Explor. Environ. Anal.* **2005**, *5*, 247–253. [[CrossRef](#)]
104. Scott, K.M.; Radford, N.W. Rutile compositions at the big bell Au deposit as a guide for exploration. *Geochem. Explor. Environ. Anal.* **2007**, *7*, 353–361. [[CrossRef](#)]
105. Meneghel, L. The occurrence of uranium in the Katanga system of northwestern Zambia. *Econ. Geol.* **1981**, *76*, 56–98. [[CrossRef](#)]
106. Porter, J.; McNaughton, N.J.; Evans, N.J.; McDonald, B.J. Rutile as a pathfinder for metals exploration. *Ore Geol. Rev.* **2020**, *120*, 103406. [[CrossRef](#)]
107. Plavsa, D.; Reddy, S.M.; Agangi, A.; Clark, C.; Kylander-Clark, A.; Tiddy, C.J. Microstructural, trace element and geochronological characterization of TiO₂ polymorphs and implications for mineral exploration. *Chem. Geol.* **2018**, *476*, 130–149. [[CrossRef](#)]
108. Huang, D.H.; Du, A.D.; Wu, C.Y.; Liu, L.S.; Sun, Y.L.; Zou, X.Q. Metallochronology of molybdenum (-copper) deposits in the North China platform: Re–Os age of molybdenite and its geological significance. *Miner. Depos.* **1996**, *15*, 365–373. (In Chinese)
109. Geng, Y.G.; Jian, W.; Li, H.Y. Re–Os Isotopic Dating of Molybdenite from Bizigou Cu deposit in Zhongtiao Mountain and Its Implication. *J. Jilin Univ. Earth Sci. Ed.* **2017**, *47*, 1405–1418.
110. Brenan, J.M.; Cherniak, D.J.; Rose, L.A. Diffusion of osmium in pyrrhotite and pyrite: Implications for closure of the Re–Os isotopic system. *Earth Planet. Sci. Lett.* **2000**, *180*, 399–413. [[CrossRef](#)]
111. Selby, D.; Creaser, R.A.; Hart, C.J.R.; Rombach, C.S.; Thompson, J.F.H.; Smith, M.T.; Bakke, A.A.; Goldfarb, R.J. Absolute timing of sulfide and gold mineralization: A comparison of Re–Os molybdenite and Ar–Ar mica methods from the Tintina Gold Belt, Alaska. *Geology* **2002**, *30*, 791–794. [[CrossRef](#)]
112. Nozaki, T.; Kato, Y.; Suzuki, K. Re–Os geochronology of the Imori Besshi-type massive sulfide deposit in the Sanbagawa metamorphic belt, Japan. *Geochim. Cosmochim. Acta* **2010**, *74*, 4322–4331. [[CrossRef](#)]
113. Coggon, J.A.; Nowell, G.M.; Pearson, D.G.; Oberthür, T.; Lorand, J.P.; Melcher, F.; Parman, S.W. The 190Pt–186Os decay system applied to dating platinum-group element mineralization of the Bushveld Complex, South Africa. *Chem. Geol.* **2012**, *302–303*, 48–60. [[CrossRef](#)]
114. Mei, H.L. Metamorphic P–T–t paths and tectonic evolution of early Proterozoic rocks from the Zhongtiao Mountains, Southern Shanxi. *Geol. Rev.* **1994**, *40*, 36–47. (In Chinese)
115. Stein, H.; Scherstén, A.; Hannah, J.; Markey, R. Subgrain-scale decoupling of Re and ¹⁸⁷Os and assessment of laser ablation ICP–MS spot dating in molybdenite. *Geochim. Cosmochim. Acta* **2003**, *67*, 3673–3686. [[CrossRef](#)]
116. Parrish, R.R. U–Pb dating of monazite and its application to geological problems: *Can. J. Earth Sci.* **1990**, *27*, 1431–1450. [[CrossRef](#)]
117. Turlin, F.; Eglinger, A.; Vanderhaeghe, O.; André-Mayer, A.S.; Poujol, M.; Mercadier, J.; Ryan, B. Synmetamorphic Cu remobilization during the Pan-African orogeny: Microstructural, petrological and geochronological data on the kyanite-micaschists hosting the Cu–(U) Lumwana deposit in the Western Zambian Copperbelt of the Lufilian belt. *Ore Geol. Rev.* **2016**, *75*, 52–75. [[CrossRef](#)]
118. Zhao, G.C.; Wilde, S.A.; Sun, M.; Guo, J.H.; Kröner, A.; Li, S.Z.; Li, X.P.; Zhang, J. Shrimp U–Pb zircon geochronology of the Huai’an Complex: Constraints on Late Archean to Paleoproterozoic magmatic and metamorphic events in the Trans-North China Orogen. *Am. J. Sci.* **2008**, *308*, 270–303. [[CrossRef](#)]
119. Wilde, S.A.; Zhao, G.C.; Wang, K.Y.; Sun, M. First SHRIMP zircon U–Pb ages for Hutuo Group in Wutaishan: Further evidence for Palaeoproterozoic amalgamation of North China Craton. *Chin. Sci. Bull.* **2004**, *49*, 83–90. [[CrossRef](#)]
120. Zhang, J.; Zhao, G.C.; Li, S.Z.; Sun, M.; Liu, S.W.; Xia, X.P.; He, Y.H. U–Pb zircon dating of the granitic conglomerates of the Hutuo Group: Affinities to the Wutai granitoids and significance to the tectonic evolution of the Trans-North China Orogen. *Acta Geol. Sin.* **2006**, *80*, 886–898. [[CrossRef](#)]
121. Faure, M.; Trap, P.; Lin, W.; Monie, P.; Bruguier, O. Polyorogenic evolution of the Paleoproterozoic Trans-North China Belt: New insights from the Luliangshan–Hengshan–Wutaishan and Fuping massifs. *Episodes* **2007**, *30*, 96–107. [[CrossRef](#)]
122. Liu, C.H.; Zhao, G.C.; Sun, M.; Zhang, J.; He, Y.H.; Yin, C.Q.; Wu, F.Y.; Yang, J.H. U–Pb and Hf isotopic study of detrital zircons from the Hutuo Group in the Trans-North China Orogen and tectonic implications. *Gondwana Res.* **2011**, *20*, 106–121. [[CrossRef](#)]
123. Liu, C.H.; Zhao, G.C.; Sun, M.; Wu, F.Y.; Yang, J.H.; Yin, C.Q.; Leung, W.H. U–Pb and Hf isotopic study of detrital zircons from the Yejiashan Group of the Lüliang Complex: Constraints on the timing of collision between the Eastern and Western blocks, North China Craton. *Sediment. Geol.* **2011**, *236*, 129–140. [[CrossRef](#)]
124. Li, Q.G.; Chen, X.; Liu, S.W.; Wang, Z.Q.; Zhou, Y.K.; Zhang, J.; Wang, T. Evaluating the Provenance of Metasedimentary rocks of the Jiangxian Group from the Zhongtiao Mountain using whole rock geochemistry and detrital zircon Hf isotope. *Acta Geol. Sin.* **2009**, *83*, 550–561. [[CrossRef](#)]

125. Zhang, J.; Zhao, G.C.; Li, S.Z.; Sun, M.; Wilde, S.A.; Liu, S.W.; Yin, C.Q. Polyphase deformation of the Fuping Complex, Trans-North China Orogen: Structures, SHRIMP U-Pb zircon ages and tectonic implications. *J. Struct. Geol.* **2009**, *31*, 177–193. [[CrossRef](#)]
126. Guan, H.; Sun, M.; Wilde, S.A.; Zhou, X.H.; Zhai, M.G. SHRIMP UPb zircon geochronology of the Fuping Complex: Implications for formation and assembly of the North China Craton. *Precambrian Res.* **2002**, *113*, 1–18. [[CrossRef](#)]
127. Compilation Group of the Geology of Copper Deposits of the Zhongtiao Mountains. *Geology of Copper Deposits in the Zhongtiao Mountains*; Geological Publishing House: Beijing, China, 1978; pp. 25–86. (In Chinese)